

1 **Title:**

2 **Neural correlates of individual odor preference in *Drosophila***

3

4 **Authors:**

5 Matthew A. Churgin<sup>1,2,\*</sup>, Danylo O. Lavrentovich<sup>1,2,\*</sup>, Matthew A. Smith<sup>1,2,10</sup>, Ruixuan  
6 Gao<sup>3,4,5,11</sup>, Edward S. Boyden<sup>3,4,6,7,8,9</sup>, Benjamin de Bivort<sup>1,2,†</sup>

7

8 **Affiliations:**

9 <sup>1</sup>Organismic and Evolutionary Biology, Harvard University, Cambridge, MA 02138, USA

10 <sup>2</sup>Center for Brain Science, Harvard University, Cambridge, MA 02138, USA

11 <sup>3</sup>McGovern Institute, MIT, Cambridge, MA 02139, USA

12 <sup>4</sup>MIT Media Lab, MIT, Cambridge, MA 02139, USA

13 <sup>5</sup>Janelia Research Campus, Howard Hughes Medical Institute, Ashburn, VA 20147, USA

14 <sup>6</sup>Department of Biological Engineering, MIT, Cambridge, MA 02142, USA

15 <sup>7</sup>Koch Institute, Department of Biology, MIT, Cambridge, MA 02139, USA

16 <sup>8</sup>Howard Hughes Medical Institute, Chevy Chase, MD 20815, USA

17 <sup>9</sup>Department of Brain and Cognitive Sciences, MIT, Cambridge, MA 02139, USA

18 <sup>10</sup>Present address: Department of Entomology, University of Wisconsin-Madison, Madison  
19 WI, 53706, USA

20 <sup>11</sup>Present address: Department of Biological Sciences/Chemistry, University of Illinois  
21 Chicago, Chicago, IL 60607, USA

22 \*These authors contributed equally

23 †Lead Contact: [debivort@oeb.harvard.edu](mailto:debivort@oeb.harvard.edu)

24 **Abstract**

25 Behavior varies even among genetically identical animals raised in the same environment.  
26 However, little is known about the circuit or anatomical origins of this individuality. We show  
27 individual *Drosophila* odor preferences (odor-vs-air and odor-vs-odor) are predicted by  
28 idiosyncratic calcium dynamics in olfactory receptor neurons (ORNs) and projection neurons  
29 (PNs), respectively. Variation in ORN presynaptic density also predicts odor-vs-odor preference.  
30 The ORN-PN synapse appears to be a locus of individuality where microscale variation gives  
31 rise to idiosyncratic behavior. Finally, simulating microscale stochasticity in ORN-PN synapses  
32 of a 3,062 neuron model of the antennal lobe recapitulates patterns of variation in PN calcium  
33 responses matching experiments. Our results demonstrate how physiological and microscale  
34 structural circuit variations can give rise to individual behavior, even when genetics and  
35 environment are held constant.

36

37 **Keywords:** individuality, neural circuits, sensory processing, olfaction, behavioral preference,  
38 variation, *Drosophila*, antennal lobe, calcium imaging, expansion imaging

## 39 Introduction

40 Individuality is a fundamental aspect of behavior that is observed even among genetically-  
41 identical animals reared in similar environments. We are specifically interested in individuality  
42 that is evident as idiosyncratic differences in behavior that persist for much of an animal's  
43 lifespan. Such variability is observed across species including round worms (Stern et al., 2017),  
44 aphids (Schuett et al., 2011), fish (Laskowski et al., 2022), mice (Freund et al., 2013), and people  
45 (Johnson et al., 2010). Small, genetically tractable model species, such as *Drosophila*, are  
46 particularly promising for discovering the genetic and neural circuit basis of individual behavior  
47 variation. Flies exhibit individuality in many behaviors (Werkhoven et al., 2021), and the  
48 mechanistic origins of this variation has been studied for phototactic preference (Kain et al.,  
49 2012), temperature preference (Kain et al., 2015), locomotor handedness (Ayroles et al., 2015;  
50 Buchanan et al., 2015; de Bivort et al., 2022), object-fixated walking (Linneweber et al., 2020),  
51 and odor preference (Honegger et al., 2019). Generally, the neural substrates of individuality are  
52 poorly understood, though in a small number of instances nanoscale circuit correlates of  
53 individual behavioral biases have been identified (Linneweber et al., 2020; Skutt-Kakaria et al.,  
54 2019). We hypothesize that as sensory cues are encoded and transformed to produce motor  
55 outputs, their representation in the nervous system becomes increasingly idiosyncratic and  
56 predictive of individual behavioral responses. We seek to identify “loci of individuality” – sites  
57 at which this idiosyncrasy emerges.

58  
59 Olfaction in the fruit fly *Drosophila melanogaster* is an amenable sensory system for identifying  
60 loci of individuality, as 1) individual odor preferences can be recorded readily, 2) neural  
61 representations of odors can be measured via calcium imaging, 3) the circuit elements of the  
62 pathway are well-established, and 4) a deep genetic toolkit enables mechanism-probing  
63 experiments. The neuroanatomy of the olfactory system, from the antenna through its first  
64 central-brain processing neuropil, the antennal lobe (AL), is broadly stereotyped across  
65 individuals (Couto et al., 2005; Grabe et al., 2015; Wilson et al., 2004). The AL features ~50  
66 anatomically identifiable microcircuits called glomeruli (Figure 1A). Each glomerulus represents  
67 an odor-coding channel and receives axon inputs from olfactory receptor neurons (ORNs)  
68 expressing the same olfactory receptor gene (de Bruyne et al., 2001). Uniglomerular projection  
69 neurons (PNs) carry odor information from each glomerulus deeper into the brain (Jeanne and  
70 Wilson, 2015). AL-intrinsic local neurons (LNs) project among glomeruli (Chou et al., 2010)  
71 and modulate odor representations (Wilson and Laurent, 2005). Glomerular organization is a key  
72 stereotype of the AL; using glomeruli as landmarks, one can identify comparable ORN axons  
73 and PNs across individuals.

74  
75 Several possible determinants of individual odor preference can already be hypothesized for the  
76 fly olfactory circuit (Rihani and Sachse, 2022). Individual flies differ in their PN calcium  
77 responses to identical odor stimuli, as well as their odor-vs-odor preference choices (Honegger et  
78 al., 2019). The extent of preference variability depends on dopamine and serotonergic

79 modulation (Honegger et al., 2019). Neuromodulation clearly plays a role in the regulation of  
80 behavioral individuality (Maloney, 2021), but its effects vary by modulator and behavior (de  
81 Bivort et al., 2022; Kain et al., 2012). With respect to wiring variation, the number of ORNs and  
82 PNs innervating a given glomerulus varies within hemispheres (Tobin et al., 2017) and across  
83 individuals (Grabe et al., 2016; Schlegel et al., 2020), as does the glomerulus-innervation pattern  
84 of individual LNs (Chou et al., 2010). Subpopulations of LNs and PNs express variable serotonin  
85 receptors (Sizemore and Dacks, 2016), so the effects of neuromodulation and wiring may  
86 interact to influence individuality. Little is known about possible molecular or nanoscale  
87 correlates of individual behavioral bias. Thus, individual odor preference could have its origins  
88 in many potential mechanisms, ranging from circuit wiring to modulation to neuronal intrinsic  
89 properties.

90  
91 Outside the olfactory system, there are two instances in which microscale circuit variation is  
92 known to predict individual behavioral preference. Wiring asymmetry in an individual fly's  
93 dorsal cluster neurons is predictive of the straightness of its object-oriented walking behavior  
94 (Linneweber et al., 2020), and left-right asymmetry in the density of presynaptic sites of  
95 protocerebral bridge - lateral accessory lobe-projecting neurons predicts an individual fly's  
96 idiosyncratic turning bias (Skutt-Kakaria et al., 2019).

97  
98 In this work, we sought to identify loci of individuality by measuring odor preferences and  
99 neural responses to odors in the same individuals and asking whether the latter predicted the  
100 former. We found that idiosyncratic calcium responses in specific neurons were predictive of  
101 olfactory preferences – variation in ORN responses predicts odor-vs-air preference; variation in  
102 PN responses predicts odor-vs-odor preference. Zooming into a molecular component, variation  
103 in the scaffolding protein Bruchpilot in ORN presynaptic terminals is also predictive of odor  
104 preference variation. To unify these results and connect wiring variation to circuit outputs, we  
105 simulated developmental variation in a 3,062-neuron spiking model of the antennal lobe.  
106 Simulated stochasticity in the ORN-PN synapse recapitulated our empirical findings. Thus, we  
107 identified the ORN-PN synapse as a locus of individuality in fly odor preference, demonstrating  
108 that behaviorally-relevant variation in neural circuits can be found in the sensory periphery at the  
109 nanoscale.

## 110 111 **Results**

### 112 *Individual flies encode odors idiosyncratically*

113 Focusing on behavioral variation within a genotype, we used isogenic animals expressing the  
114 fluorescent calcium reporter GCamp6m (Chen et al., 2013) in either of the two most peripheral  
115 neural subpopulations of the *Drosophila* olfactory circuit, ORNs or PNs (Figure 1E). We  
116 performed head-fixed 2-photon calcium imaging after measuring odor preference in an  
117 untethered assay (Honegger et al., 2019) (Figure 1B-D, Figure 1 – figure supplement 1A).

118 Individual odor preferences are stable over timescales longer than this experiment (Figure 1 –  
119 figure supplement 1B-E).

120

121 We measured volumetric calcium responses in the antennal lobe (AL), where ORNs synapse  
122 onto PNs in ~50 discrete microcircuits called glomeruli (Figure 1A) (Couto et al., 2005; Grabe et  
123 al., 2015). Flies were stimulated with a panel of 12 odors plus air (Figure 1D, Figure 1 – figure  
124 supplement 2) and *k*-means clustering was used to automatically segment the voxels of 5  
125 glomeruli from the resulting 4-D calcium image stacks (Figure 1E, Figure 1 – figure supplement  
126 4, Materials and Methods) (Couto et al., 2005). Both ORN and PN odor responses were roughly  
127 stereotyped across individuals (Figure 1G,H), but also idiosyncratic (Honegger et al., 2019).  
128 Responses in PNs appeared to be more idiosyncratic than ORNs (Figure 1J); a logistic linear  
129 classifier decoding fly identity from glomerular responses was more accurate when trained on  
130 PN than ORN responses (Figure 1 – figure supplement 5A). While the responses of single ORNs  
131 are known to vary more than those of single PNs (Wilson, 2013), our recordings represent the  
132 total response of all ORNs or PNs in a glomerulus. This might explain our observation that  
133 ORNs exhibited less idiosyncrasy than PNs. PN responses were more variable within flies, as  
134 measured across the left and right hemisphere ALs, compared to ORN responses (Figure 1 –  
135 figure supplement 5C), consistent with the hypothesis that odor representations become more  
136 idiosyncratic farther from the sensory periphery.

137

### 138 *Individual ORN responses predict odor-air preference*

139 Next we analyzed the relationship of idiosyncratic coding to odor preference, by asking in which  
140 neurons (if any) did calcium responses predict individual preferences of flies choosing between  
141 air and an aversive odor (3-octanol, OCT; Figure 1 – figure supplement 1B; Supplementary  
142 Video 1). Because we could potentially predict preference (a single value) using numerous  
143 glomerular-odor predictors, and had a limited number of observations (dozens), we used  
144 dimensional reduction to make parsimonious predictions. We computed the principal  
145 components (PCs) of the glomerulus-odor responses (in either ORNs or PNs) across individuals  
146 (Figure 1G-I; Figure 1 – figure supplement 3, Figure 1 – figure supplement 7) and fit linear  
147 models to predict the behavior of individual flies from their values on the odor response PCs. PC  
148 1 of ORN activity was a significant predictor of odor preference ( $r = 0.48$ ;  $p = 0.0099$ ; Figure  
149 1K,L). PC 1 of PN activity was also correlated with odor preference in separate model training  
150 and testing experiments (Figure 2 – figure supplement 1; statistics from combined train and test  
151 data:  $r = 0.29$ ,  $p = 0.035$ , Figure 1K,M). Our interpretation is that ORN responses are  
152 idiosyncratic and predict individual odor-vs-air preference, and that these idiosyncrasies are  
153 transmitted to PNs, where they remain predictive of behavioral responses.

154

155 How should we interpret the calcium PCs only predicting odor preference with  $r = \sim 0.4$ ? This  
156 value falls short of 1.0 due to at least two factors: 1) any non-linearity in the relationship between  
157 calcium responses and behavior, and 2) sampling error in, and temporal instability of, behavior

158 and calcium responses over the duration of the experiment. A lower bound on the latter can be  
159 estimated from the repeatability of behavioral measures over time (Figure 1 – figure supplement  
160 1B-E). To disentangle these effects, we performed a statistical analysis that estimated model  
161 performance in the absence of sampling error and drift in the measurement of behavior and  
162 calcium responses, i.e., the strength of the linear relationship between latent behavior and  
163 calcium states (Figure 4 – figure supplement 1; Materials and Methods). This analysis implies  
164 the nominal correlation of 0.48 between behavior and PC1 of ORN calcium responses  
165 corresponds to a correlation between latent calcium and behavior states ( $\rho_{signal}$ ) of 0.64. This  
166 makes intuitive sense because the raw model  $R^2$  (0.23) is close to the behavior repeatability  $R^2$   
167 (0.27), an upper-limit on model performance (Figure 1 – figure supplement 1B). The model  
168 predicting odor-vs-air behavior from PC1 of PN calcium responses has an estimated  $\rho_{signal}$  of  
169 0.40 (Figure 4).

170

171 *PN, but not ORN, responses predict odor-odor preference*

172 Variation in the sensory periphery has been previously implicated as a driver of behavioral  
173 variation (Michelson et al., 2017; Osborne et al., 2005), but we wondered whether ORNs would  
174 be a locus of individuality for a behavior requiring the comparison of two odors (rather than just  
175 the sensation of a single odor). So we next determined if idiosyncratic calcium responses could  
176 predict individual preferences in an odor-vs-odor choice (Figure 1 – figure supplement 1D,E;  
177 (Honegger et al., 2019); Supplementary Video 2), specifically between the aversive  
178 monomolecular odorants (OCT) and 4-methylcyclohexanol (MCH). We assessed if any of the  
179 first 5 PCs of PN calcium responses was a linear predictor of individual odor-vs-odor  
180 preferences. PC 2 accounted for 15% of preference variance in a training set of 47 flies (Figure 2  
181 – figure supplement 1C). This PC 2-based model explained 31% of preference variance on test  
182 data (n=22 flies) (Figure 2 – figure supplement 1D). Combined train/test statistics ( $r = 0.45$ ;  $p =$   
183  $0.0001$ ) are presented in Figure 1N,P. We estimate that the correlation between between latent  
184 PN calcium and odor-vs-odor behavioral states is  $\rho_{signal} = 0.75$  (Figure 4).

185

186 No PCs of ORN neural activity could linearly predict odor preference beyond the level of  
187 shuffled controls (n=35 flies) (Figure 1N,O; Figure 4). The best ORN PC model only predicted  
188 odor-vs-odor behavior with a nominal  $R^2$  of 0.031 ( $\rho_{signal} = 0.30$ ). Projecting ORN data onto PC  
189 2 of PN responses (the successful model) did not predict odor-vs-odor behavior ( $R^2=0.060$ ).  
190 Therefore, whereas idiosyncratic ORN responses (and PN responses) were predictive of odor-vs-  
191 air preferences, only PN responses were predictive of odor-vs-odor preferences.

192

193 We next sought an intuitive understanding of the models linking calcium responses and odor  
194 preference. The loadings of the ORN and PN PCs indicate that variation across individuals was  
195 correlated at the level of glomeruli much more strongly than odorant (Figure 1 – figure  
196 supplements 3, 7). This suggests that stochastic variation in the olfactory circuit results in  
197 individual-level fluctuations in the responses of glomeruli-specific rather than odor-specific



198 responses. In the case of the odor-vs-air model, the PC 1 loadings of both ORN and PN neural  
199 activity were non-negative across all glomerulus-odor response dimensions (Figure 2A,D),  
200 apparently representing each individual's total response in all glomerulus-odorant combinations.  
201 Indeed, a linear model that simply sums all calcium responses in ORNs (Figure 2B,E) predicted  
202 behavior with  $R^2=0.25$  ( $\rho_{signal} = 0.67$ ); for PN responses, it was somewhat predictive, though less  
203 so ( $R^2=0.098$ ;  $\rho_{signal} = 0.43$ ). For both ORNs and PNs, the model's slope parameter ( $\beta$ ) was  
204 negative (Table 1), meaning that stronger AL responses correlated with stronger preference for  
205 air, consistent with OCT being aversive. Thus, flies whose ORNs and PNs respond, as a  
206 population, more strongly to OCT are more likely to avoid it.

207  
208 In the odor-vs-odor preference model, the loadings of PC2 of PN calcium responses contrast the  
209 responses of the DM2 and DC2 glomeruli with opposing weights (Figure 2G), suggesting that  
210 the activation of DM2 relative to DC2 predicts the likelihood of a fly preferring OCT to MCH.  
211 Indeed, a linear model constructed from the total DM2 minus total DC2 PN response (Figure 2H)  
212 predicted individual preference for OCT versus MCH ( $R^2=0.12$ ;  $\rho_{signal} = 0.59$ ; Figure 2I). The  
213 model beta coefficient was negative (Table 1), indicating that greater activation of DM2 vs DC2  
214 correlates with preference for MCH. With respect to odor-vs-odor behavior, we conclude that the  
215 relative responses of DM2 vs DC2 in PNs largely explains an individual's preference.

216  
217 Odor experience has been shown to modulate subsequent AL responses (Golovin and Broadie,  
218 2016; Iyengar et al., 2010; Sachse et al., 2007). This raises the possibility that our models were  
219 actually predicting individual flies' past odor experiences (i.e., the specific pattern of odor  
220 stimulation flies received in the behavioral assay) rather than their preferences. To address this,  
221 we imposed the specific odor experiences of previously tracked untethered flies (in the odor-vs-  
222 odor assay) on naive "yoked" control flies (Figure 2J) and measured PN odor responses of the  
223 yoked flies. Applying the PN PC 2 model to the yoked calcium responses did not predict flies'  
224 odor experience ( $R^2=0.019$ ; Figure 2K). Thus, the responses of DM2 vs DC2 in PNs do not  
225 predict individual open-loop odor experiences.

226  
227 Previous work found that PN response transients, rather than fixed points, contain more odor  
228 identity information (Mazor and Laurent, 2005). We therefore asked at which times during odor  
229 presentation an individual's neural responses could best predict odor preference. Applying each  
230 of our three successful calcium-to-behavior models (ORN PC1-odor-vs-air, PN PC1-odor-vs-air,  
231 PN PC2-odor-vs-odor) to the time-varying calcium signals, we found that in all cases, behavior  
232 prediction generally rose during odor delivery (Figure 4 – figure supplement 2A-C). In ORNs,  
233 the predictive accuracy remained high after odor offset, whereas in PNs it declined. Thus, the  
234 overall sensitivity of ORNs that appears to predict odor-vs-air preferences may persist after odor  
235 stimulation ends. The times during which calcium responses predicted individual behavior  
236 generally aligned to the times during which a linear classifier could decode odor identity from

237 ORN or PN responses (Figure 4 – figure supplement 2D), suggesting that idiosyncrasies in odor  
238 encoding predict individual preferences.

239

#### 240 *Variation in a presynaptic scaffolding protein predicts odor-odor preference variation*

241 We next investigated how structural variation in the nervous system might underlie the variations  
242 in neural activity that correlate with idiosyncratic behavior. Because PN, but not ORN, calcium  
243 responses predicted odor-vs-odor preference, we hypothesized that a circuit element between  
244 ORNs to PNs could confer onto PNs behaviorally-relevant physiological idiosyncrasies absent in  
245 ORNs. We therefore imaged presynaptic T-bar density in ORNs using transgenic mStrawberry-  
246 tagged Brp-Short, immunohistochemistry and confocal microscopy (Mosca and Luo, 2014) after  
247 measuring individual preference for OCT versus MCH (Figure 3A). Brp-Short density was  
248 quantified as fluorescence intensity / glomerulus volume for 4 of the 5 focus glomeruli (Figure  
249 3B, Figure 3 – figure supplement 1A-F; DL5 was not readily segmentable across samples, but  
250 was dispensable in all behavior-predicting models). This measure was consistent across  
251 hemispheres (Figure 3 – figure supplement 1C), while also showing variation among individuals.

252

253 To begin assessing the relationship between presynaptic structural variation and behavior, we  
254 calculated the principal components of Brp-Short density across individuals. PCs 1 and 2 were  
255 qualitatively similar to those in our calcium imaging experiments: PC 1 was non-negative  
256 positive across glomeruli, reflecting global average staining intensity, and PC 2 exhibited a sign  
257 contrast between DC2 loadings and all other glomerulus loadings (Figure 3 – figure supplement  
258 1G). As in the PN calcium response models, PC 2 of Brp-Short density was the best predictor of  
259 odor-vs-odor preferences in training data (Figure 3D-E, Figure 3 – figure supplement 1I,  $R^2 =$   
260  $0.22$ ,  $n=22$  flies) and for test data (Figure 3 – figure supplement 1J,  $R^2 = 0.078$ ,  $n=31$  flies;  
261 statistics from combined train and test data:  $R^2 = 0.088$ ,  $n=53$  flies, Figure 3F). We tested our  
262 intuitive hypothesis that PC 2 captures the differential response of DM2 vs DC2 by applying the  
263 “DM2 minus DC2 model” (Figure 2H) to the Brp-Short data (Figure 3G). While this  
264 rudimentary model did not attain statistical significance, it had a negative beta coefficient,  
265 implying that higher presynaptic density in DM2 compared to DC2 correlates with preference for  
266 MCH (Table 1), consistent with the beta parameter of the PN calcium response model.

267

268 The range of differences between DM2 and DC2 Brp-Short staining across individuals (-50% to  
269 40%; normalized by the average of the two glomeruli) was less than that of PN calcium response  
270 differences (-60% to 100%; Figure 3 – figure supplement 2), suggesting that presynaptic density  
271 variation is not the full explanation of calcium response variability. Consistently, the best  
272 presynaptic density models are less predictive of behavior than the best calcium response models  
273 ( $R^2=0.088$  vs  $R^2=0.22$ ;  $\rho_{signal} = 0.51$  and  $0.75$ , respectively; Figure 2 – figure supplement 1C,D  
274 vs Figure 3 – figure supplement 1I,J). Nevertheless, differences in presynaptic inputs to DM2  
275 and DC2 PNs may contribute to variation in DM2 and DC2 calcium dynamics, in turn giving rise  
276 to individual preferences for OCT versus MCH.



277

278 To help formulate hypotheses about what variable Brp-Short staining represented on a  
279 microstructural level, we performed paired behavior and expansion microscopy (Asano et al.,  
280 2018; Gao et al., 2019) in flies expressing Brp-Short specifically in DC2-projecting ORNs  
281 (Supplementary Video 3). Expansion yielded a ~4-fold increase in linear resolution, allowing  
282 imaging of individual Brp-Short puncta (Figure 3 – figure supplement 1K) (Gao et al., 2019).  
283 While the sample size (n=8) of this imaging pipeline did not warrant a formal modeling analysis,  
284 the trend between density of Brp-Short in DC2 and odor-vs-odor preference was more consistent  
285 with a positive correlation than the trend between Brp-Short volume and odor-vs-odor preference  
286 (Figure 3 – figure supplement L,M). These results hint that variation in the density of Bruchpilot  
287 protein within presynaptic sites, rather than other biophysical properties, may be a critical factor  
288 underlying physiological and behavioral individuality.

289

290 *Developmental stochasticity in a simulated AL recapitulates empirical PN response variation*  
291 Finally, we sought an integrative understanding of how synaptic variation plays out across the  
292 olfactory circuit to produce behaviorally-relevant physiological variation. We developed a leaky-  
293 integrate-and-fire model of the entire AL, comprising 3,062 spiking neurons and synaptic  
294 connectivity taken directly from the *Drosophila* hemibrain connectome (Scheffer et al., 2020).  
295 After tuning the model to perform canonical AL computations, we introduced different kinds of  
296 stochastic variations to the circuit and determined which (if any) would produce the patterns of  
297 idiosyncratic PN response variation observed in our calcium imaging experiments (Figure 5A).  
298 This approach assesses potential mechanisms linking developmental variation in synapses to  
299 physiological variation that apparently drives behavioral individuality.

300

301 The biophysical properties of neurons in our model (Figure 5B, Table 2) were determined by  
302 published electrophysiological studies (See *Voltage model* in Materials and Methods) and were  
303 similar to those used in previous fly models (Kakaria and de Bivort, 2017; Pisokas et al., 2020).  
304 The polarity of neurons was determined largely by their cell type (ORNs are excitatory, PNs  
305 predominantly excitatory, and LNs predominantly inhibitory – explained further in Materials and  
306 Methods). The strength of synaptic connections between any pair of AL neurons was given by  
307 the hemibrain connectome (Scheffer et al., 2020) (Figure 5C). Odor inputs were simulated by  
308 injecting current into ORNs to produce spikes in those neurons at rates that match published  
309 ORN-odor recordings (Münch and Galizia, 2016), and the output of the system was recorded as  
310 the firing rates of PNs during odor stimulation (Figure 5D). At this point, there remained only  
311 four free parameters in our model, the relative sensitivity (postsynaptic current per upstream  
312 action potential) of each AL cell type (ORNs, PNs, excitatory LNs and inhibitory LNs). We  
313 explored this parameter space manually, and identified a configuration in which AL simulation  
314 (Figure 5 – figure supplement 1) recapitulated four canonical properties seen experimentally  
315 (Figure 5 – figure supplement 2): 1) typical firing rates at baseline and during odor stimulation  
316 (Bhandawat et al., 2007; Dubin and Harris, 1997; Jeanne and Wilson, 2015; Seki et al., 2010), 2)

317 a more uniform distribution of PN firing rates compared to ORN rates (Bhandawat et al., 2007),  
318 3) greater separation of PN odor representations compared to ORN representations (Bhandawat  
319 et al., 2007), and 4) a sub-linear transfer function between ORNs and PNs (Bhandawat et al.,  
320 2007). Thus, our simulated AL appeared to perform the fundamental computations of real ALs,  
321 providing a baseline for assessing the effects of idiosyncratic variation.

322  
323 We simulated stochastic individuality in the AL circuit in two ways (Figure 5E): 1) glomerular-  
324 level variation in PN input-synapse density (reflecting a statistical relationship observed between  
325 glomerular volume and synapse density in the hemibrain, Figure 5 – figure supplement 4), and 2)  
326 bootstrapping of neuronal compositions within cell types (reflecting variety in developmental  
327 program outcomes for ORNs, PNs, etc.). Supplementary Video 4 shows the diverse connectivity  
328 matrices attained under these resampling approaches. We simulated odor responses in thousands  
329 of ALs made idiosyncratic by these sources of variation, and in each, recorded the firing rates of  
330 PNs when stimulated by the 12 odors from our experimental panel (Figure 5F, Figure 5 – figure  
331 supplement 1).

332  
333 To determine which sources of variation produced patterns of PN coding variation consistent  
334 with our empirical measurements, we compared principal components of PN responses from real  
335 idiosyncratic flies to those of simulated idiosyncratic ALs. Empirical PN responses are strongly  
336 correlated at the level of glomeruli (Figure 5G; Figure 1 – figure supplement 7). As a positive  
337 control that the model can recapitulate this empirical structure, resampling PN input-synapse  
338 density across glomeruli produced PN response correlations strongly organized by glomerulus  
339 (Figure 5I). As a negative control, variation in PN responses due solely to poisson timing of  
340 ORN input spikes (i.e., absent any circuit idiosyncrasy) was not organized at the glomerular level  
341 (Figure 5H). Strikingly, bootstrapping ORN membership yielded a strong glomerular  
342 organization in PN responses (Figure 5J). The loadings of the top PCs under ORN bootstrapping  
343 are dominated by responses of a single glomerulus to all odors, including DM2 and DC2. This is  
344 reminiscent of PC2 of PN calcium responses, with prominent (opposite sign) loadings for DM2  
345 and DC2. Bootstrapping LNs, in contrast, produced much less glomerular organization (Figure  
346 5K), with little resemblance to the loadings of the empirical calcium PCs. The PCA loadings for  
347 simulated PN responses under all combinations of cell type bootstrapping and PN input-synapse  
348 density resampling are given in Figure 5 – figure supplement 5.

349  
350 DM2 and DC2 (also DL5) stand out in the PCA loadings under PN input-synapse density  
351 resampling and ORN bootstrapping (Figure 5I,J), suggesting that behaviorally-relevant PN  
352 coding variation is recapitulated in this modeling framework. To formalize this analysis, for each  
353 idiosyncratic AL, we computed a “behavioral preference” by applying the PN PC2 linear model  
354 (Figure 1N,P) to simulated PN responses. We then determined how accurately a linear classifier  
355 could distinguish OCT- vs MCH-preferring ALs in the space of the first 3 PCs of PN responses  
356 (Figure 5 – figure supplement 6). High accuracy was attained under PN input-synapse density

357 resampling and ORN bootstrapping (sources of circuit variation that produced PN response  
358 loadings highlighting DM2 and DC2). Thus, developmental variability in ORN populations may  
359 drive patterns of PN physiological variation that in turn drive individuality in odor-vs-odor  
360 choice behavior.

361

362

## 363 **Discussion**

364 We found elements of the *Drosophila* olfactory circuit where patterns of physiological activity  
365 emerge that are predictive of individual behavioral preferences. These circuit elements can be  
366 considered loci of individuality, as they appear to harbor the origins of idiosyncratic preferences  
367 among isogenic animals reared in the same environment. Specifically, the total responsiveness of  
368 ORNs predicts idiosyncratic odor-vs-air preferences, and contrasting glomerular activation in  
369 PNs predicts idiosyncratic odor-vs-odor preferences (Figures 1, 2). Both of these circuit elements  
370 are in the olfactory sensory periphery, suggesting that behavioral idiosyncrasy arises early in the  
371 sensorimotor transformation. We were particularly surprised at the extent to which PN activity  
372 could predict preference between two aversive odors. We estimated that the strength of the  
373 correlation between latent PN activity and behavioral states was 0.75 (Figure 4B).

374

375 Previous work has found mammalian peripheral circuit areas are predictive of individual  
376 behavior (Britten et al., 1996; Michelson et al., 2017; Newsome et al., 1989; Osborne et al.,  
377 2005), but this study is among the first (Linneweber et al., 2020; Mellert et al., 2016; Skutt-  
378 Kakaria et al., 2019) to link cellular-level circuit variants and individual behavior in the absence  
379 of genetic variation. Another key conclusion is that loci of individuality are likely to vary, even  
380 within the sensory periphery, with the specific behavioral paradigm (i.e., odor-vs-odor or odor-  
381 vs-air). Our ability to predict behavioral preferences was limited by the repeatability of the  
382 behavior itself (Figure 4 – figure supplement 1). Low persistence of odor preference may be  
383 attributable to factors like internal states or plasticity. It may be fruitful in future studies to map  
384 circuit elements whose activity predicts trial-to-trial behavioral fluctuations within individuals.

385

386 Seeking insight into the molecular basis of behaviorally-relevant physiological variation, we  
387 imaged Brp in the axon terminals of the ORN-PN synapse, using confocal and expansion  
388 microscopy. Brp glomerular (and probably puncta) density was a predictor of individual odor-vs-  
389 odor preferences (Figure 3). Higher Brp in DM2 predicted stronger MCH preference, like higher  
390 calcium responses in DM2 PNs, suggesting that variation in PN inputs underlies PN  
391 physiological variation. This is consistent with the recent finding of a linear relationship between  
392 synaptic density and excitatory postsynaptic potentials (Liu et al., 2022) and another study in  
393 which idiosyncratic synaptic density in central complex output neurons predicts individual  
394 locomotor behavior (Skutt-Kakaria et al., 2019). The predictive relationship between Brp and  
395 behavior was weaker than that of PN calcium responses, suggesting there are other determinants,

396 such as other synaptic proteins, neurite morphology, or the influence of idiosyncratic LNs (Chou  
397 et al., 2010) modulating the ORN-PN transformation (Nagel et al., 2015).

398

399 To integrate our synaptic and physiological results, we implemented a spiking model with 3,062  
400 neurons and synaptic weights drawn directly from the fly connectome (Scheffer et al., 2020)  
401 (Figure 5). With light parameter tuning, this model recapitulated canonical AL computations,  
402 providing a baseline for assessing the effects of idiosyncratic stochastic variation. The apparent  
403 variation in odor responses across simulated individuals (Figure 5F) is less than that seen in the  
404 empirical calcium responses (Figure 1H), likely due to 1) biological phenomena missing from  
405 the model, 2) the lack of measurement noise, and 3) the fact that our perturbations are applied to  
406 the connectome of a single fly. When examining PCA loadings, however, simulating  
407 idiosyncratic ALs by varying PN input synapse density or bootstrapping ORNs produced  
408 correlated PN responses across odors in DC2 and DM2, matching our experimental results.  
409 These sources of variation specifically implicate the ORN-PN synapse (like our Brp results) as  
410 an important substrate for establishing behaviorally-relevant patterns of PN response variation.

411

412 The flies used in our experiments were isogenic and reared in standardized laboratory conditions  
413 that produce reduced behavioral individuality compared to enriched environments (Akhund-Zade  
414 et al., 2019; Körholz et al., 2018; Zocher et al., 2020). Yet, even these conditions yield  
415 substantial behavioral individuality. We do not expect variability in the expression of the flies'  
416 transgenes to be a major driver of this individuality, as wildtype flies have a similarly broad  
417 distribution of odor preferences (Honegger et al., 2019). The ultimate source of stochasticity in  
418 this behavior remains a mystery, with possibilities ranging from thermal fluctuations at the  
419 molecular scale to macroscopic, but seemingly irrelevant, variations like the exact fill level of the  
420 culture media (Honegger and de Bivort, 2018). Developing nervous systems employ various  
421 compensation mechanisms to dampen out the effects of these fluctuations (Marder, 2011; Tobin  
422 et al., 2017). Behavioral variation may be beneficial, supporting a bet-hedging strategy (Hopper,  
423 1999) to counter environmental fluctuations (Akhund-Zade et al., 2020; Honegger et al., 2019;  
424 Kain et al., 2015; Krams et al., 2021). Empirically, the net effect of dampening and accreted  
425 ontological (Gomez-Marin and Ghazanfar, 2019) fluctuations is individuals with diverse  
426 behaviors. This process unfolds across all levels of biological regulation. Just as PN response  
427 variation appears to be partially rooted in glomerular Brp variation, the latter has its own  
428 molecular roots, including, perhaps, stochasticity in gene expression (Li et al., 2017; Raj et al.,  
429 2010), itself a predictor of idiosyncratic behavioral biases (Werkhoven et al., 2021). Improved  
430 methods to longitudinally assay the fine-scale molecular and anatomical makeup of behaving  
431 organisms throughout development and adulthood will be invaluable to further illuminate the  
432 mechanistic origins of individuality.

433

## 434 **Materials and Methods**

435

### 436 ***Data and code availability***

437 All raw data, totaling 600 GB, are available via hard drive from the authors. A smaller (7 GB)  
438 repository with partially processed data files and MATLAB/Python scripts sufficient to generate  
439 figures and results is available at Zenodo ([doi:10.5281/zenodo.8092972](https://doi.org/10.5281/zenodo.8092972)).

440

### 441 ***Fly rearing***

442 Experimental flies were reared in a *Drosophila* incubator (Percival Scientific DR-36VL) at 22°  
443 C, 40% relative humidity, and 12:12h light:dark cycle. Flies were fed cornmeal/dextrose  
444 medium, as previously described (Honegger et al., 2019). Mated female flies aged 3 days post-  
445 eclosion were used for behavioral persistence experiments. Mated female flies aged 7 to 15 days  
446 post-eclosion were used for all paired behavior-calcium imaging and immunohistochemistry  
447 experiments.

448

### 449 ***Fly stocks***

450 The following stocks were obtained from the Bloomington *Drosophila* Stock Center:  
451 P{20XUAS-IVS-GCaMP6m}attP40 (BDSC #42748), w[\*]; P{w[+mC]=Or13a-GAL4.F}40.1  
452 (BDSC #9945), w[\*]; P{w[+mC]=Or19a-GAL4.F}61.1 (BDSC #9947), w[\*];  
453 P{w[+mC]=Or22a-GAL4.7.717}14.2 (BDSC #9951), w[\*]; P{w[+mC]=Orco-GAL4.W}11.17;  
454 TM2/TM6B, Tb[1] (BDSC #26818). Transgenic lines were outcrossed to the isogenic line  
455 isokh11 (Honegger et al., 2019) for at least 5 generations prior to being used in any experiments.  
456 GH146-Gal4 was a gift provided by Y. Zhong (Honegger et al., 2019). w; UAS-Brp-Short-  
457 mStrawberry; UAS-mCD8-GFP; + was a gift of Timothy Mosca and was not outcrossed to the  
458 isokh11 background (Mosca and Luo, 2014).

459

### 460 ***Odor delivery***

461 Odor delivery during behavioral tracking and neural activity imaging was controlled with  
462 isolation valve solenoids (NResearch Inc.) (Honegger et al., 2019). Saturated headspace from 40  
463 ml vials containing 5 ml pure odorant were serially diluted via carbon-filtered air to generate a  
464 variably (10-25%) saturated airstream controlled by digital flow controllers (Alicat Scientific)  
465 and presented to flies at total flow rates of ~100 mL/min. The odor panel used for imaging was  
466 comprised of the following odorants: 2-heptanone (CAS #110-43-0, Millipore Sigma), 1-  
467 pentanol (CAS #71-41-0, Millipore Sigma), 3-octanol (CAS #589-98-0, Millipore Sigma), hexyl-  
468 acetate (CAS #142-92-7, Millipore Sigma), 4-methylcyclohexanol (CAS #589-91-3, Millipore  
469 Sigma), pentyl acetate (CAS #628-63-7, Millipore Sigma), 1-butanol (CAS #71-36-3, Millipore  
470 Sigma), ethyl lactate (CAS #97-64-3, Millipore Sigma), geranyl acetate (CAS #105-87-3,  
471 Millipore Sigma), 1-hexanol (CAS #111-27-34, Millipore Sigma), citronella java essential oil (  
472 191112, Aura Cacia), and 200 proof ethanol (V1001, Decon Labs).

473



474 ***Odor preference behavior***

475 Odor preference was measured at 25°C and 20% relative humidity. As previously described  
476 (Honegger et al., 2019), individual flies confined to custom-fabricated tunnels were illuminated  
477 with infrared light and behavior was recorded with a digital camera (Basler) and zoom lens  
478 (Pentax). The odor choice tunnels were 50 mm long, 5 mm wide, and 1.3 mm tall. Custom real-  
479 time tracking software written in MATLAB was used to track centroid, velocity, and principal  
480 body axis angle throughout the behavioral experiment, as previously described (Honegger et al.,  
481 2019). After a 3-minute acclimation period, odorants were delivered to either end of the tunnel  
482 array for 3 minutes. Odor preference score was calculated as the fraction of time spent in the  
483 reference side of the tunnel during odor-on period minus the time spent in the reference side of  
484 the tunnel during the pre-odor acclimation period.

485

486 ***Behavioral preference persistence measurements***

487 After measuring odor preference, flies were stored in individual housing fly plates (modified 96-  
488 well plates; FlySorter, LLC) on standard food, temperature, humidity, and lighting conditions.  
489 Odor preference of the same individuals was measured 3 and/or 24 hours later. In some cases, fly  
490 tunnel position was randomized between measurements. We observed that randomization had  
491 little effect on preference persistence.

492

493 ***Calcium imaging***

494 Flies expressing GCaMP6m in defined neural subpopulations were imaged using a custom-built  
495 two-photon microscope and ultrafast Ti:Sapphire laser (Spectra-Physics Mai Tai) tuned to 930  
496 nm, at a power of 20 mW out of the objective (Olympus XLUMPlanFL N 20x/1.00 W). For  
497 paired behavior and imaging experiments, the time elapsed between behavior measurement and  
498 imaging ranged from 15 minutes to 3 hours. Flies were anesthetized on ice and immobilized in  
499 an aluminum sheet with a female-fly-sized hole cut in it. The head cuticle between the antennae  
500 and ocelli was removed along with the tracheae to expose the ALs from the dorsal side. Volume  
501 scanning was performed using a piezoelectric objective mount (Physik Instrumente). ScanImage  
502 2013 software (Vidrio Technologies) was used to coordinate galvanometer laser scanning and  
503 image acquisition. Custom Matlab (Mathworks) scripts were used to coordinate image  
504 acquisition and control odor delivery. 256 by 192 (x-y) pixel 16-bit tiff images were recorded.  
505 The piezo travel distance was adjusted between 70 and 90  $\mu\text{m}$  so as to cover most of the AL. The  
506 number of z-sections in a given odor panel delivery varied between 7 and 12 yielding a volume  
507 acquisition rate of 0.833 Hz. Odor delivery occurred from 6-9.6s of each recording.

508

509 Each fly experienced up to four deliveries of the odor panel. The antennal lobe being recorded  
510 (left or right) was alternated after each successful completion of an odor panel. Odors were  
511 delivered in randomized order. In cases where baseline fluorescence was very weak or no  
512 obvious odor responses were visible, not all four panels were delivered.

513



514 ***Glomerulus segmentation and labeling***

515 Glomerular segmentation masks were extracted from raw image stacks using a *k*-means  
516 clustering algorithm based on time-varying voxel fluorescence intensities, as previously  
517 described (Honegger et al., 2019). Each image stack, corresponding to a single odor panel  
518 delivery, was processed individually. Time-varying voxel fluorescence values for each odor  
519 delivery were concatenated to yield a voxel-by-time matrix consisting of each voxel's recorded  
520 value during the course of all 13 odor deliveries of the odor panel. After z-scoring, principal  
521 component analysis was performed on this matrix and 75% of the variance was retained. Next, *k*-  
522 means (*k*=80, 50 replicates with random starting seeds) was performed to produce 50 distinct  
523 voxel cluster assignment maps which we next used to calculate a consensus map. This approach  
524 was more accurate than clustering based on a single *k*-means seed.

525  
526 Of the 50 generated voxel cluster assignment maps, the top 5 were selected by choosing those  
527 maps with the lowest average within-cluster sum of distances, selecting for compact glomeruli.  
528 The remaining maps were discarded. Next, all isolated voxel islands in each of the top 5 maps  
529 were identified and pruned based on size (minimum size = 100 voxels, maximum size = 10000  
530 voxels). Finally, consensus clusters were calculated by finding voxel islands with significant  
531 overlap across all 5 of the pruned maps. Voxels which fell within a given cluster across all 5  
532 pruned maps were added to the consensus cluster. This process was repeated for all clusters until  
533 the single consensus cluster map was complete. In some cases we found by manual inspection  
534 that some individual glomeruli were clearly split into two discrete clusters. These splits were  
535 remedied by automatically merging all consensus clusters whose centroids were separated by a  
536 physical distance of less than 30 voxels and whose peak odor response Spearman correlation was  
537 greater than 0.8. Finally, glomeruli were manually labeled based on anatomical position,  
538 morphology, and size (Grabe et al., 2015). We focused our analysis on 5 glomeruli (DM1, DM2,  
539 DM3, DL5, and DC2), which were the only glomeruli that could be observed in all paired  
540 behavior-calcium datasets. However, not all 5 glomeruli were identified in all recordings (Figure  
541 1 – figure supplement 3). Missing glomerular data was later mean-imputed.

542  
543 ***Calcium image data analysis***

544 All data was processed and analyzed in MATLAB 2018a (Mathworks). Calcium responses for  
545 each voxel were calculated as  $\Delta f/f = [f(t) - F]/F$ , where *f*(*t*) and *F* are the instantaneous and  
546 average fluorescence, respectively. Each glomerulus' time-dependent calcium response was  
547 calculated as the mean  $\Delta f/f$  across all voxels falling within the glomerulus' automatically-  
548 generated segmentation mask during a single volume acquisition. Time-varying odor responses  
549 were normalized to baseline by subtracting the median of pre-odor  $\Delta f/f$  from each trace. Peak  
550 odor response was calculated as the maximum fluorescence signal from 7.2s to 10.8s (images 6  
551 through 9) of the recording.

552

553 To compute principal components of calcium dynamics, each fly's complement of odor panel  
554 responses (a 5 glomeruli by 13 odors = 65-dimensional vector) was concatenated. Missing  
555 glomerulus-odor response values were filled in with the mean glomerulus-odor pair across all fly  
556 recordings for which the data was not missing. After infilling, principal component analysis was  
557 carried out with individual odor panel deliveries as observations and glomerulus-odor responses  
558 pairs as features.

559  
560 Inter- and intra-fly distances (Figure 1J) were calculated using the projections of each fly's  
561 glomerulus-odor responses onto all principal components. For each fly, the average Euclidean  
562 distance between response projections 1) among left lobe trials, 2) among right lobe trials, and 3)  
563 between left and right lobe trials were averaged together to get a single within-fly distance. Intra-  
564 fly distances were computed in a similar fashion (for each fly, taking the average distance of its  
565 response projections to those of other flies using only left lobe trials / only right lobe trials /  
566 between left-right trials, then averaging these three values to get a single across-fly distance).

567  
568 In a subset of experiments in which we imaged calcium activity, some solenoids failed to open,  
569 resulting in the failure of odor delivery in a small number of trials. In these cases, we identified  
570 trials with valve failures by manually recognizing that glomeruli failed to respond during the  
571 nominal odor period. These trials were treated as missing data and infilled, as described above.  
572 Fewer than ~10% of flies and 5% of odor trials were affected.

573  
574 For all predictive models constructed, the average principal component score or glomerulus-odor  
575  $\Delta f/f$  response across trials was used per individual; that is, each fly contributed one data point to  
576 the relevant model. Linear models were constructed from behavior scores and the relevant  
577 predictor (principal component, average  $\Delta f/f$  across dimensions, specific glomerulus  
578 measurements) as described in the text and Tables 1-2. 95% confidence intervals around model  
579 regression lines were estimated as  $\pm 2$  standard deviations of the value of the regression line at  
580 each x-position across 2000 bootstrap replicates (resampling flies). To predict behavior as a  
581 function of time during odor delivery, we analyzed data as described above, but considered only  
582  $\Delta f/f$  at each single time point (Figure 4 – figure supplement 2A-C), rather than averaging during  
583 the peak response interval.

584  
585 To decode individual identity from neural responses, we first performed PCA on individual odor  
586 panel peak responses. We retained principal component scores constituting specified fractions of  
587 variance (Figure 1 – figure supplement 5A) and trained a linear logistic classifier to predict  
588 individual identity from single odor panel deliveries.

589  
590 To decode odor identity from neural responses, each of the 5 recorded glomeruli were used as  
591 features, and the calcium response of each glomerulus to a specific odor at a specified time point  
592 were used as observations (PNs, n=5317 odor deliveries; ORNs, n=2704 odor deliveries). A

593 linear logistic classifier was trained to predict the known odor identity using 2-fold cross-  
594 validation. That is, a model was trained on half the data and evaluated on the remaining half, and  
595 then this process was repeated with the train and test half reversed. The decoding accuracy was  
596 quantified as the fraction of odor deliveries in which the predicted odor was correct.

597

### 598 ***Inference of correlation between latent calcium and behavior states***

599 We performed a simulation-based analysis to infer the strength of the correlation between latent  
600 calcium (Brp) and behavior states, given the  $R^2$  of a given linear model. Figure 4 – figure  
601 supplement 1A is a schematic of the data generation process we assume underlies our observed  
602 data. We assume that the “true” behavioral and calcium values of the animal are captured by  
603 unobserved latent states  $X_c$  and  $X_b$ , respectively, such that the correlation between  $X_c$  and  $X_b$  is the  
604 biological signal captured by the model, having adjusted for the noise associated with actually  
605 measuring behavior and calcium ( $\rho_{signal}$ ). Our calcium and odor preference scores are subject to  
606 measurement error and temporal instability (behavior and neural activity were measured 1-3  
607 hours apart). These effects are both noise with respect to estimating the linear relationship  
608 between calcium and behavior. Their magnitude can be estimated using the empirical  
609 repeatability of behavior and calcium experiments respectively. Thus, our overall approach was  
610 to assume true latent behavior and calcium signals that are correlated at the level  $\rho_{signal}$ , add noise  
611 to them commensurate with the repeatability of these measures to simulate measured behavior  
612 and calcium, and record the simulated empirical  $R^2$  between these measured signals. This was  
613 done many times to estimate distributions of empirical  $R^2$  given  $\rho_{signal}$ . These distributions could  
614 finally be used in the inverse direction to infer  $\rho_{signal}$  given the actual model  $R^2$  values computed  
615 in our study.

616

617 Specifically, we simulated  $X_c$  as a set of  $N$  standard normal variables ( $N$  equalling the number of  
618 flies used to compute a correlation between predicted and measured preference) and generated  $X_b$   
619  $= \rho_{signal} X_c + (1 - \rho_{signal}^2 Z)^{1/2}$ , where  $Z$  is a set of  $N$  standard normal variables uncorrelated with  $X_c$ , a  
620 procedure that ensures that  $corr(X_c, X_b) = \rho_{signal}$ . Next, we simulated observed calcium readouts  
621  $X_c'$  and  $X_c''$ , such that  $corr(X_c, X_c') = corr(X_c, X_c'') = r_c$ . Similarly, we simulated noisy observed  
622 behavioral assay readouts  $X_b'$  and  $X_b''$ , such that  $corr(X_b, X_b') = corr(X_b, X_b'') = r_b$ . The values  
623 of  $r_c$  and  $r_b$  were fixed by the empirical repeatability of calcium ( $R_{c,c^2}$ ) and behavior ( $R_{b,b^2}$ )  
624 respectively as follows. Since calcium is a multidimensional measure, and our calcium model  
625 predictors are based on principal components of glomerulus-odor responses, we used variance  
626 explained along the PCs to calculate a single value for the calcium repeatability  $R_{c,c^2}$ . We  
627 compared the eigenvalues of the real calcium PCA to those of shuffled calcium data (shuffling  
628 glomerulus/odor responses for each individual fly), computing  $R_{c,c^2}$  by summing the variance  
629 explained along the PCs of the calcium data up until the component-wise variance for the  
630 calcium data fell below that of the shuffled data, a similar approach as done in Berman et al.,  
631 2014 and Werkhoven et al., 2021.  $R_{c,c^2}$  was calculated to be 0.77 for both ORN and PN calcium;  
632 we set  $r_c = (R_{c,c^2})^{1/4}$  to ensure  $corr(X_c', X_c'')^2 = R_{c,c^2}$ . We matched  $r_b$  to the repeatability across

633 odor preference trials in the same flies measured 3h apart ( $R_{b,b^2}=0.23$  for OCT vs AIR, and 0.12  
634 for OCT vs MCH, Figure 1 – figure supplement 1B-D), setting  $r_b = (R_{b,b^2})^{1/4}$  to ensure  $\text{corr}(X_b',$   
635  $X_b'')^2 = R_{b,b^2}$ .

636  
637 We varied  $\rho_{\text{signal}}$  from 0 to 1 in increments of 0.01, and for each  $\rho_{\text{signal}}$ , we simulated a set of  $N$   $X_c$   
638 and generated  $X_b, X_c', X_c'', X_b',$  and  $X_b''$ , then we computed a simulated observed calcium-  
639 behavior relationship strength  $R_{c,b^2} = \text{corr}(X_c', X_b')^2$ . We repeated this simulation 10,000 times  
640 for each  $\rho_{\text{signal}}$  and plotted the resultant relationship between  $\rho_{\text{signal}}$  against  $R_{c,b^2}$  (percentiles of  
641  $R_{c,b^2}$  are displayed in Figure 4 – figure supplement 1B). Then, for each linear model of interest,  
642 we inferred  $\rho_{\text{signal}}$  by extracting the marginal distribution of  $\rho_{\text{signal}}$  near the model's  $R^2$  (+/- 20%)  
643 and report the median  $\rho_{\text{signal}}$ .

644  
645 The procedure outlined above was done analogously for models using Brp-short relative  
646 fluorescence intensity, performing the PCA-based calcium response repeatability step with PCA  
647 on the multidimensional Brp-short relative fluorescence intensity (which yielded  $R_{brp,brp^2} =$   
648 0.75).

#### 649 **DoOR data**

651 DoOR data for the glomeruli and odors relevant to our study was downloaded from  
652 <http://neuro.uni-konstanz.de/DoOR/default.html> (Münch and Galizia, 2016).

#### 653 **Yoked odor experience experiments**

655 We selected six flies for which both odor preference and neural activity were recorded to serve  
656 as the basis for imposed odor experiences for yoked control flies. The experimental flies were  
657 chosen to represent a diversity of preference scores. Each experimental fly's odor experience was  
658 binned into discrete odor bouts to represent experience of either MCH or OCT based on its  
659 location in the tunnel as a function of time (Figure 2J). Odor bouts lasting less than 100 ms were  
660 omitted due to limitations on odor-switching capabilities of the odor delivery apparatus. To  
661 deliver a given experimental fly's odor experience to yoked controls, we set both odor streams  
662 (on either end of the tunnel apparatus) to deliver the same odor experienced by the experimental  
663 fly at that moment during the odor-on period. No odor was delivered to yoked controls during  
664 time points in which the experimental fly resided in the tunnel choice zone (central 5 mm). See  
665 Figure 2J for an example pair of experimental fly and yoked control behavior and odor  
666 experience.

#### 667 **Immunohistochemistry**

669 After measuring odor preference behavior, 7-15 day-old flies were anesthetized on ice and brains  
670 were dissected in phosphate buffered saline (PBS). Dissection and immunohistochemistry were  
671 carried out as previously reported (Wu and Luo, 2006). The experimenter was blind to the  
672 behavioral scores of all individuals throughout dissection, imaging, and analysis. Individual

673 identities were maintained by fixing, washing, and staining each brain in an individual 0.2 mL  
674 PCR tube using fluid volumes of 100 uL per brain (Fisher Scientific). Primary incubation  
675 solution contained mouse anti-nc82 (1:40, DSHB), chicken anti-GFP (1:1000, Aves Labs), rabbit  
676 anti-mStrawberry (1:1000, biorbyt), and 5% normal goat serum (NGS, Invitrogen) in PBT (0.5%  
677 Triton X-100 in PBS). Secondary incubation solution contained Atto 647N-conjugated goat anti-  
678 mouse (1:250, Millipore Sigma), Alexa Fluor 568-conjugated goat anti-rabbit (1:250), Alexa  
679 Fluor 488-conjugated goat anti-chicken (1:250, ThermoFisher), and 5% NGS in PBT. Primary  
680 and secondary incubation times were 2 and 3 overnights, respectively, at 4° C. Stained samples  
681 were mounted and cleared in Vectashield (H-1000, Vector Laboratories) between two coverslips  
682 (12-568B, Fisher Scientific). Two reinforcement labels (5720, Avery) were stacked to create a  
683 0.15 mm spacer.

684

### 685 ***Expansion microscopy***

686 Immunohistochemistry for expansion microscopy was carried out as described above, with the  
687 exception that antibody concentrations were modified as follows: mouse anti-nc82 (1:40),  
688 chicken anti-GFP (1:200), rabbit anti-mStrawberry (1:200), Atto 647N-conjugated goat anti-  
689 mouse (1:100), Alexa Fluor 568-conjugated goat anti-rabbit (1:100), Alexa Fluor 488-conjugated  
690 goat anti-chicken (1:100). Expansion of stained samples was performed as previously described  
691 (Asano et al., 2018; Gao et al., 2019). Expanded samples were mounted in coverslip-bottom petri  
692 dishes (MatTek Corporation) and anchored by treating the coverslip with poly-l-lysine solution  
693 (Millipore Sigma) as previously described (Asano et al., 2018).

694

### 695 ***Confocal imaging***

696 All confocal imaging was carried out at the Harvard Center for Biological Imaging. Unexpanded  
697 samples were imaged on an LSM700 (Zeiss) inverted confocal microscope equipped with a 40x  
698 oil-immersion objective (1.3 NA, EC Plan Neofluar, Zeiss). Expanded samples were imaged on  
699 an LSM880 (Zeiss) inverted confocal microscope equipped with a 40x water-immersion  
700 objective (1.1 NA, LD C-Apochromat, Zeiss). Acquisition of Z-stacks was automated with Zen  
701 Black software (Zeiss).

702

### 703 ***Standard confocal image analysis***

704 We used custom semi-automated code to generate glomerular segmentation masks from confocal  
705 z-stacks of unexpanded Orco>Brp-Short brains. Using Matlab, each image channel was median  
706 filtered ( $\sigma_x, \sigma_y, \sigma_z = 11, 11, 1$  pixels) and downsampled in x and y by a factor of 11. Next, an  
707 ORN mask was generated by multiplying and thresholding the Orco>mCD8 and Orco>Brp-Short  
708 channels. Next, a locally normalized nc82 and Orco>mCD8 image stack were multiplied and  
709 thresholded, and the ORN mask was applied to remove background and other undesired brain  
710 structures. This pipeline resulted in a binary image stack which maximized the contrast of the  
711 glomerular structure of the antennal lobe. We then applied a binary distance transform and



712 watershed transform to generate discrete subregions which aimed to represent segmentation  
713 masks for each glomerulus tagged by Orco-Gal4.

714

715 However, this procedure generally resulted in some degree of under-segmentation; that is, some  
716 glomerular segmentation masks were merged. To split each merged segmentation mask, we  
717 convolved a ball (whose radius was proportional to the cube root of the volume of the  
718 segmentation mask in question) across the mask and thresholded the resulting image. The  
719 rationale of this procedure was that 2 merged glomeruli would exhibit a mask shape resembling  
720 two touching spheres, and convolving a similarly-sized sphere across this volume followed by  
721 thresholding would split the merged object. After ball convolution, we repeated the distance and  
722 watershed transform to once more generate discrete subregions representing glomerular  
723 segmentation masks. This second watershed step generally resulted in over-segmentation; that is,  
724 by visual inspection it was apparent that many glomeruli were split into multiple subregions.  
725 Therefore, we finally manually agglomerated the over-segmented subregions to generate single  
726 segmentation masks for each glomerulus of interest. We used a published atlas to aid manual  
727 identification of glomeruli (Grabe et al., 2015). The total Brp-Short fluorescence signal within  
728 each glomerulus was determined and divided by the volume of the glomerulus' segmentation  
729 mask to calculate Brp-Short density values.

730

### 731 *Expansion microscopy image analysis*

732 The spots function in Imaris 9.0 (Bitplane) was used to identify individual Brp-Short puncta in  
733 expanded sample image stacks of Or13a>Brp-Short samples (Mosca and Luo, 2014). The spot  
734 size was set to 0.5  $\mu\text{m}$ , background subtraction and region-growing were enabled, and the default  
735 spot quality threshold was used for each image stack. Identified spots were used to mask the Brp-  
736 Short channel and the resultant image was saved as a new stack. In MATLAB, a glomerular  
737 mask was generated by smoothing ( $\sigma_x, \sigma_y, \sigma_z = 40, 40, 8$  pixels) and thresholding (92.5th  
738 percentile) the raw Brp-Short image stack. The mask was then applied to the spot image stack to  
739 remove background spots. Finally, the masked spot image stack was binarized and spot number  
740 and properties were quantified.

741

### 742 *Antennal Lobe modeling*

743 We constructed a model of the antennal lobe to test the effect of circuit variation on PN activity  
744 variation across individuals. Our general approach to producing realistic circuit activity with the  
745 AL model was 1) using experimentally-measured parameters whenever possible (principally the  
746 connectome wiring diagram and biophysical parameters measured electrophysiologically), 2)  
747 associating free parameters only with biologically plausible categories of elements, while  
748 minimizing their number, and 3) tuning the model using those free parameters so that it  
749 reproduced high-level patterns of activity considered in the field to represent the canonical  
750 operations of the AL. Simulations were run in Python (version 3.6) (van Rossum and Drake,  
751 2011), and model outputs were analyzed using Jupyter notebooks (Kluyver et al., 2016) and



752 Python and Matlab scripts.

753

### 754 ***AL model neurons***

755 Release 1.2 of the hemibrain connectomics dataset (Scheffer et al., 2020) was used to set the  
756 connections in the model. Hemibrain body IDs for ORNs, LNs, and PNs were obtained via the  
757 lists of neurons supplied in the supplementary tables in Schlegel et al., 2020. ORNs and PNs of  
758 non-olfactory glomeruli (VP1d, VP1l, VP1m, VP2, VP3, VP4, VP5) were ignored, leaving 51  
759 glomeruli. Synaptic connections between the remaining 2574 ORNs, 197 LNs, 166 mPNs, and  
760 130 uPNs were queried from the hemibrain API. All ORNs were assigned to be excitatory  
761 (Wilson, 2013). Polarities were assigned to PNs based on the neurotransmitter assignments in  
762 Bates et al., 2020. mPNs without neurotransmitter information were randomly assigned an  
763 excitatory polarity with probability equal to the fraction of neurotransmitter-identified mPNs that  
764 are cholinergic; the same process was performed for uPNs. After confirming that the model's  
765 output was qualitatively robust to which mPNs and uPNs were randomly chosen, this random  
766 assignment was performed once and then frozen for subsequent analyses.

767

768 Of the 197 LNs, we assigned 31 to be excitatory, based on the estimated 1:5.4 ratio of eLNs to  
769 iLNs in the AL (Tsai et al., 2018). To account for observations that eLNs broadly innervate the  
770 AL (Shang et al., 2007), all LNs were ranked by the number of innervated glomeruli, and the 31  
771 eLNs were chosen uniformly at random from the top 50% of LNs in the list. This produced a  
772 distribution of glomerular innervations in eLNs qualitatively similar to that of *krasavietz* LNs in  
773 Supplementary Figure 6 of Chou et al., 2010.

774

### 775 ***Voltage model***

776 We used a single-compartment leaky-integrate-and-fire voltage model for all neurons as in  
777 Kakaria and de Bivort, 2017, in which each neuron had a voltage  $V_i(t)$  and current  $I_i(t)$ . When the  
778 voltage of neuron  $i$  was beneath its threshold  $V_{i,thr}$ , the following dynamics were obeyed:

779

$$780 \quad C_i \frac{dV_i}{dt} = \frac{V_{i,0} - V_i(t)}{R_i} + I_{i,odor}(t) + \sum_{j=1}^N a_j W_{ji} I_j(t)$$

781

782 Each neuron  $i$  had electrical properties: membrane capacitance  $C_i$ , resistance  $R_i$ , and resting  
783 membrane potential  $V_{i,0}$  with values from electrophysiology measurements (Table 2).

784

785 When the voltage of a neuron exceeded the threshold  $V_{i,thr}$ , a templated action potential was  
786 filled into its voltage time trace, and a templated postsynaptic current was added to all  
787 downstream neurons, following the definitions in Kakaria and de Bivort, 2017.

788

789 Odor stimuli were simulated by triggering ORNs to spike at frequencies matching known  
790 olfactory receptor responses to the desired odor. The timing of odor-evoked spikes was given by

791 a Poisson process, with firing rate  $FR$  for ORNs of a given glomerulus governed by:

792

$$793 \quad FR_{glom,odor}(t) = FR_{max} D_{glom,odor} (f_a + (1 - f_a)e^{-t/t_a})$$

794

795  $FR_{max}$ , the maximum ORN firing rate, was set to 400 Hz.  $D_{glom,odor}$  is a value between 0 and 1  
796 from the DoOR database, representing the response of an odorant receptor/glomerulus to an  
797 odor, estimated from electrophysiology and/or fluorescence data (Münch and Galizia, 2016).

798 ORNs display adaptation to odor stimuli (Wilson, 2013), captured by the final term with

799 timescale  $t_a = 110 \text{ ms}$  to 75% of the initial value, as done in Kao and Lo, 2020. Thus, the

800 functional maximum firing rate of an ORN was 75% of 400 Hz = 300 Hz, matching the highest

801 ORN firing rates observed experimentally (Hallem et al., 2004). After determining the times of

802 ORN spikes according to this firing-rate rule, spikes were induced by the addition of  $10^6$

803 picoamps in a single time step. This reliably triggered an action potential in the ORN, regardless

804 of currents from other neurons. In the absence of odors, spike times for ORNs were drawn by a

805 Poisson process at 10 Hz, to match reported spontaneous firing rates (de Bruyne et al., 2001).

806

807 For odor-glomeruli combinations with missing DoOR values (40% of the dataset), we performed

808 imputation via alternating least squares (using the `pca` function with option ‘als’ to infill missing

809 values ([MATLAB documentation](#)) on the odor x glomerulus matrix 1000 times and taking the

810 mean infilled matrix, which provides a closer match to ground truth missing values than a single

811 run of ALS (Figure 1 – figure supplement 5 of Werkhoven et al., 2021).

812

813 A neuron  $j$  presynaptic to  $i$  supplies its current  $I_j(t)$  scaled by the synapse strength  $W_{ji}$ , the

814 number of synapses in the hemibrain dataset from neuron  $j$  to  $i$ . Rows in  $W$  corresponding to

815 neurons with inhibitory polarity (i.e. GABAergic PNs or LNs) were set negative. Finally, post-

816 synaptic neurons (columns of the connectivity matrix) have a class-specific multiplier  $a_i$ , a hand-

817 tuned value, described below.

818

### 819 ***AL model tuning***

820 Class-specific multiplier current multipliers ( $a_i$ ) were tuned using the panel of 18 odors from

821 Bhandawat et al., 2007 (our source for several experimental observations of high-level AL

822 function): benzaldehyde, butyric acid, 2,3-butanedione, 1-butanol, cyclohexanone, Z3-hexenol,

823 ethyl butyrate, ethyl acetate, geranyl acetate, isopentyl acetate, isoamyl acetate, 4-methylphenol,

824 methyl salicylate, 3-methylthio-1-propanol, octanal, 2-octanone, pentyl acetate, E2-hexenal,

825 trans-2-hexenal, gamma-valerolactone. Odors were “administered” for 400 ms each, with 300 ms

826 odor-free pauses between odor stimuli.

827

828 The high-level functions of the AL that represent a baseline, working condition were: (1) firing

829 rates for ORNs, LNs, and PNs matching the literature (listed in Table 2 and see (Bhandawat et

830 al., 2007; Dubin and Harris, 1997; Jeanne and Wilson, 2015; Seki et al., 2010), (2) a more

831 uniform distribution of PN firing rates during odor stimuli compared to ORN firing rates, (3)  
832 greater separation of representations of odors in PN-coding space than in ORN-coding space, and  
833 (4) a sublinear transfer function between ORN firing rates and PN firing rates. Features (2) - (4)  
834 relate to the role of the AL in enhancing the separability of similar odors (Bhandawat et al.,  
835 2007).

836  
837 To find a parameterization with those functions, we tuned the values of  $a_i$  as scalar multipliers on  
838 ORN, eLN, iLN, and PN columns of the hemibrain connectivity matrix. Thus, these values  
839 represent cell type-specific sensitivities to presynaptic currents, which may be justified by the  
840 fact that ORNs/LNs/PNs are genetically distinct cell populations (McLaughlin et al., 2021; Xie  
841 et al., 2021). A grid search of the four class-wise sensitivity parameters produced a configuration  
842 that reasonably satisfied the above criteria (Figure 5 – figure supplement 2). In this  
843 configuration, the ORN columns of the hemibrain connectivity matrix are scaled by 0.1, eLNs by  
844 0.04, iLNs by 0.02, and PNs by 0.4. The relatively large multiplier on PNs is potentially  
845 consistent with the fact that PNs are sensitive to small differences between weak ORN inputs  
846 (Bhandawat et al., 2007). Model outputs were robust over several different sets of  $a_i$ , provided  
847 iLN sensitivity  $\approx$  eLN < ORN < PN.

848  
849 We analyzed the sensitivity of the model's parameters around their baseline values of  $a_{ORN}$ ,  $a_{eLN}$ ,  
850  $a_{iLN}$ ,  $a_{PN} = (0.1, 0.04, 0.02, 0.4)$ . Each parameter was independently scaled up to 4x or 1/4x of its  
851 baseline value (Figure 5 – figure supplement 3), and the PN firing rates recorded. Separately,  
852 multiple-parameter manipulations were performed by multiplying each parameter by a random  
853 log-Normal value with mean 1 and +/-1 standard deviation corresponding to a 2x or 0.5x scaling  
854 on each parameter. Mean PN-odor responses were calculated for all manipulated runs and  
855 compared to the mean PN-odor responses for the baseline configuration. A manipulation effect  
856 size was calculated by cohen's  $d$  ((mean manipulated response - mean baseline response)/(pooled  
857 standard deviation)). None of these manipulations reached effect size magnitudes larger than 0.9  
858 (which can be roughly interpreted as the number of standard deviations in the baseline PN  
859 responses away from the mean baseline PN response), which signaled that the model was robust  
860 to the sensitivity parameters in this range. The most sensitive parameter was, unsurprisingly,  $a_{PN}$ .

861  
862 Notable ways in which the model behavior deviates from experimental recordings (and thus  
863 caveats on the interpretation of the model) include: 1) Model LNs appear to have more  
864 heterogeneous firing rates than real LNs, with many LNs inactive for this panel of odor stimuli.  
865 This likely reflects a lack of plastic/homeostatic mechanisms in the model to regularize LN firing  
866 rates given their variable synaptic connectivity (Chou et al., 2010). 2) Some PNs had off-odor  
867 rates that are high compared to real PNs, resulting in a distribution of ON-OFF responses that  
868 had a lower limit than in real recordings. Qualitatively close matches were achieved between the  
869 model and experimental data in the distributions of odor representations in ORN vs PN spaces  
870 and the non-linearity of the ORN-PN transfer function.

871

## 872 ***AL model circuit variation generation***

873 We generated AL circuit variability in two ways: cell-type bootstrapping, and synapse density  
874 resampling. These methods assume that the distribution of circuit configurations across  
875 individual ALs can be generated by resampling circuit components within a single individual's  
876 AL (neurons and glomerular synaptic densities, respectively, from the hemibrain EM volume).

877

878 To test the effect of variation in the developmental complement of neurons of particular types,  
879 we bootstrapped populations of interest from the list of hemibrain neurons. Resampling with  
880 replacement of ORNs was performed glomerulus-by-glomerulus, i.e., separately among each  
881 pool of ORNs expressing a particular *Odorant receptor* gene. The same was done for PNs. For  
882 LNs, all 197 LNs were treated as a single pool; there was no finer operation based on LN  
883 subtypes or glomerular innervations. This choice reflects the high developmental variability of  
884 LNs (Chou et al., 2010). The number of synapses between a pair of bootstrapped neurons was  
885 equal to the synapse count between those neurons in the hemibrain connectivity matrix.

886

887 In some glomeruli, bootstrapping PNs produced unreasonably high variance in the total PN  
888 synapse count. For instance, DP1m, DC4, and DM3 each harbor PNs that differ in total synapse  
889 count by a factor of ~10. Since these glomeruli have between two to three PNs each, in a sizable  
890 proportion of bootstrap samples, all-highly connected (or all-lowly) connected PNs are chosen in  
891 such glomeruli. To remedy this biologically unrealistic outcome, we examined the relationship  
892 between total input PN synapses within a glomerulus and glomerular volume (Figure 5 – figure  
893 supplement 4). In the “synapse density resampling” method, we required that the number of PN  
894 input synapses within a glomerulus reflect a draw from the empirical relationship between total  
895 input PN synapses and glomerular volume as present in the hemibrain data set. This was  
896 achieved by, for each glomerulus, sampling from the following distribution that depends on  
897 glomerular volume, then multiplying the number of PN input synapses by a scalar to match that  
898 sampled value:

899

$$900 \quad \log S_g = \log (a V_g^d) + \varepsilon_g, \varepsilon_g \sim N(0, \sigma^2)$$

901

902 Here  $S_g$  is the PN input synapse count for glomerulus  $g$ ,  $V_g$  is the volume of glomerulus  $g$  (in  
903 cubic microns),  $\varepsilon$  is a Gaussian noise variable with standard deviation  $\sigma$ , and  $a$ ,  $d$  are the scaling  
904 factor and exponent of the volume term, respectively. The values of these parameters ( $a = 8.98$ ,  
905  $d = 0.73$ ,  $\sigma = 0.38$ ) were fit using maximum likelihood.

906

## 907 **Quantification and statistical analysis**

908 All fly behavior and calcium data was processed and analyzed in MATLAB 2018a (Mathworks).  
909 AL simulations were run in Python (version 3.6) (van Rossum and Drake, 2011), and model  
910 outputs were analyzed using Jupyter notebooks (Kluyver et al., 2016) and Python scripts. We

911 performed a power analysis prior to the study to determine that recording calcium activity in 20-  
912 40 flies would be sufficient to identify moderate calcium-behavior correlations. Sample sizes for  
913 expansion microscopy were smaller, as the experimental procedure was more involved –  
914 therefore, we did not conduct a formal statistical analysis. Linear models were fit using the fitlm  
915 MATLAB function (<https://www.mathworks.com/help/stats/fitlm.html>); coefficients and p-  
916 values of models between measured preferences and predicted preferences are listed in Table 1.  
917 95% confidence intervals around model regression lines were estimated as +/- 2 standard  
918 deviations of the value of the regression line at each x-position across 2000 bootstrap replicates  
919 (resampling flies). Boxplots depict the median value (points), interquartile range (boxes), and  
920 range of the data (whiskers).

921

### 922 **Acknowledgments**

923 We thank Asa Barth-Maron and Rachel Wilson for discussions helpful to the AL modeling, and  
924 Katrin Vogt for help revising the manuscript. Ed Soucy and Brett Graham of the Center for Brain  
925 Science Neuroengineering Core helped maintain the olfactometer and microscope. D.L. was  
926 supported by the NSF-Simons Center for Mathematical and Statistical Analysis of Biology at  
927 Harvard, award number #1764269 and the Harvard Quantitative Biology Initiative. B.L.d.B. was  
928 supported by a Klingenstein-Simons Fellowship Award, a Smith Family Odyssey Award, a  
929 Harvard/MIT Basic Neuroscience Grant, National Science Foundation grant no. IOS-1557913,  
930 and NIH/NINDS grant no. 1R01NS121874-01. E.B. was supported by a Harvard/MIT Basic  
931 Neuroscience Grant, Lisa Yang, John Doerr, and NIH grant no. 1R01EB024261.

932

### 933 **Author contributions**

934 M.C. conducted behavior experiments with assistance from M.S., conducted confocal  
935 microscopy, and conducted expansion microscopy with contributions from R. G. and E.B. D.L.  
936 implemented the computational AL model. B.L.d.B. supervised the project.

937

### 938 **Declaration of interests**

939 E.B. is a co-founder of a company that aims to commercialize expansion microscopy for medical  
940 purposes. R.G. and E.B. are co-inventors on multiple patents related to expansion microscopy.  
941 The authors declare no other competing interests.



942 **References**

- 943 Akhund-Zade J, Ho S, O’Leary C, de Bivort B. 2019. The effect of environmental enrichment on  
944 behavioral variability depends on genotype, behavior, and type of enrichment. *J Exp Biol*  
945 **222**. doi:10.1242/jeb.202234
- 946 Akhund-Zade J, Yoon D, Bangerter A, Polizos N, Campbell M, Soloshenko A, Zhang T, Wice  
947 E, Albright A, Narayanan A, Schmidt P, Saltz J, Ayroles J, Klein M, Bergland A, de Bivort  
948 B. 2020. Wild flies hedge their thermal preference bets in response to seasonal fluctuations.  
949 *bioRxiv*. doi:10.1101/2020.09.16.300731
- 950 Asano SM, Gao R, Wassie AT, Tillberg PW, Chen F, Boyden ES. 2018. Expansion Microscopy:  
951 Protocols for Imaging Proteins and RNA in Cells and Tissues. *Curr Protoc Cell Biol*  
952 **80**:e56. doi:10.1002/cpcb.56
- 953 Ayroles JF, Buchanan SM, O’Leary C, Skutt-Kakaria K, Grenier JK, Clark AG, Hartl DL, De  
954 Bivort BL. 2015. Behavioral idiosyncrasy reveals genetic control of phenotypic variability.  
955 *Proceedings of the National Academy of Sciences* **112**:6706–6711.
- 956 Bates AS, Schlegel P, Roberts RJV, Drummond N, Tamimi IFM, Turnbull R, Zhao X, Marin  
957 EC, Popovici PD, Dhawan S, Jamasb A, Javier A, Serratos Capdevila L, Li F, Rubin GM,  
958 Waddell S, Bock DD, Costa M, Jefferis GSXE. 2020. Complete Connectomic  
959 Reconstruction of Olfactory Projection Neurons in the Fly Brain. *Curr Biol*.  
960 doi:10.1016/j.cub.2020.06.042
- 961 Berman GJ, Choi DM, Bialek W, Shaevitz JW. 2014. Mapping the stereotyped behaviour of  
962 freely moving fruit flies. *J R Soc Interface* **11**. doi:10.1098/rsif.2014.0672
- 963 Bhandawat V, Olsen SR, Gouwens NW, Schlieff ML, Wilson RI. 2007. Sensory processing in the  
964 *Drosophila* antennal lobe increases reliability and separability of ensemble odor  
965 representations. *Nat Neurosci* **10**:1474–1482. doi:10.1038/nn1976
- 966 Britten KH, Newsome WT, Shadlen MN, Celebrini S, Movshon JA. 1996. A relationship  
967 between behavioral choice and the visual responses of neurons in macaque MT. *Vis*  
968 *Neurosci* **13**:87–100. doi:10.1017/s095252380000715x
- 969 Buchanan SM, Kain JS, de Bivort BL. 2015. Neuronal control of locomotor handedness in  
970 *Drosophila*. *Proc Natl Acad Sci U S A* **112**:6700–6705. doi:10.1073/pnas.1500804112
- 971 Cao L-H, Jing B-Y, Yang D, Zeng X, Shen Y, Tu Y, Luo D-G. 2016. Distinct signaling of  
972 *Drosophila* chemoreceptors in olfactory sensory neurons. *Proc Natl Acad Sci U S A*  
973 **113**:E902–11. doi:10.1073/pnas.1518329113
- 974 Chen T-W, Wardill TJ, Sun Y, Pulver SR, Renninger SL, Baohan A, Schreiter ER, Kerr RA,  
975 Orger MB, Jayaraman V, Looger LL, Svoboda K, Kim DS. 2013. Ultrasensitive fluorescent  
976 proteins for imaging neuronal activity. *Nature* **499**:295–300. doi:10.1038/nature12354
- 977 Chou Y-H, Spletter ML, Yaksi E, Leong JCS, Wilson RI, Luo L. 2010. Diversity and wiring  
978 variability of olfactory local interneurons in the *Drosophila* antennal lobe. *Nat Neurosci*  
979 **13**:439–449. doi:10.1038/nn.2489
- 980 Couto A, Alenius M, Dickson BJ. 2005. Molecular, anatomical, and functional organization of  
981 the *Drosophila* olfactory system. *Curr Biol* **15**:1535–1547. doi:10.1016/j.cub.2005.07.034
- 982 de Bivort B, Buchanan S, Skutt-Kakaria K, Gajda E, Ayroles J, O’Leary C, Reimers P, Akhund-  
983 Zade J, Senft R, Maloney R, Ho S, Werkhoven Z, Smith MA-Y. 2022. Precise  
984 Quantification of Behavioral Individuality From 80 Million Decisions Across 183,000 Flies.  
985 *Front Behav Neurosci* **16**:836626. doi:10.3389/fnbeh.2022.836626
- 986 de Bruyne M, Foster K, Carlson JR. 2001. Odor coding in the *Drosophila* antenna. *Neuron*



- 987           **30**:537–552. doi:10.1016/s0896-6273(01)00289-6
- 988   Dubin AE, Harris GL. 1997. Voltage-activated and odor-modulated conductances in olfactory  
989   neurons of *Drosophila melanogaster*. *Journal of Neurobiology* **32**:123–137.  
990   doi:10.1002/(SICI)1097-4695(199701)32:1<123::AID-NEU11>3.0.CO;2-L
- 991   Freund J, Brandmaier AM, Lewejohann L, Kirste I, Kritzler M, Krüger A, Sachser N,  
992   Lindenberger U, Kempermann G. 2013. Emergence of individuality in genetically identical  
993   mice. *Science* **340**:756–759. doi:10.1126/science.1235294
- 994   Gao R, Asano SM, Upadhyayula S, Pisarev I, Milkie DE, Liu T-L, Singh V, Graves A, Huynh  
995   GH, Zhao Y, Bogovic J, Colonell J, Ott CM, Zugates C, Tappan S, Rodriguez A,  
996   Mosaliganti KR, Sheu S-H, Pasolli HA, Pang S, Xu CS, Megason SG, Hess H, Lippincott-  
997   Schwartz J, Hantman A, Rubin GM, Kirchhausen T, Saalfeld S, Aso Y, Boyden ES, Betzig  
998   E. 2019. Cortical column and whole-brain imaging with molecular contrast and nanoscale  
999   resolution. *Science* **363**. doi:10.1126/science.aau8302
- 1000   Golovin RM, Broadie K. 2016. Developmental experience-dependent plasticity in the first  
1001   synapse of the *Drosophila* olfactory circuit. *J Neurophysiol* **116**:2730–2738.  
1002   doi:10.1152/jn.00616.2016
- 1003   Gomez-Marin A, Ghazanfar AA. 2019. The Life of Behavior. *Neuron* **104**:25–36.  
1004   doi:10.1016/j.neuron.2019.09.017
- 1005   Grabe V, Baschwitz A, Dweck HKM, Lavista-Llanos S, Hansson BS, Sachse S. 2016.  
1006   Elucidating the Neuronal Architecture of Olfactory Glomeruli in the *Drosophila* Antennal  
1007   Lobe. *Cell Rep* **16**:3401–3413. doi:10.1016/j.celrep.2016.08.063
- 1008   Grabe V, Strutz A, Baschwitz A, Hansson BS, Sachse S. 2015. Digital in vivo 3D atlas of the  
1009   antennal lobe of *Drosophila melanogaster*. *J Comp Neurol* **523**:530–544.  
1010   doi:10.1002/cne.23697
- 1011   Hallem EA, Ho MG, Carlson JR. 2004. The molecular basis of odor coding in the *Drosophila*  
1012   antenna. *Cell* **117**:965–979. doi:10.1016/j.cell.2004.05.012
- 1013   Honegger K, de Bivort B. 2018. Stochasticity, individuality and behavior. *Curr Biol* **28**:R8–R12.  
1014   doi:10.1016/j.cub.2017.11.058
- 1015   Honegger KS, Smith MA-Y, Churgin MA, Turner GC, de Bivort BL. 2019. Idiosyncratic neural  
1016   coding and neuromodulation of olfactory individuality in *Drosophila*. *Proc Natl Acad Sci U*  
1017   *S A*. doi:10.1073/pnas.1901623116
- 1018   Hopper KR. 1999. Risk-spreading and bet-hedging in insect population biology. *Annu Rev*  
1019   *Entomol* **44**:535–560. doi:10.1146/annurev.ento.44.1.535
- 1020   Huang Y-C, Wang C-T, Su T-S, Kao K-W, Lin Y-J, Chuang C-C, Chiang A-S, Lo C-C. 2018. A  
1021   Single-Cell Level and Connectome-Derived Computational Model of the *Drosophila* Brain.  
1022   *Front Neuroinform* **12**:99. doi:10.3389/fninf.2018.00099
- 1023   Iyengar A, Chakraborty TS, Goswami SP, Wu C-F, Siddiqi O. 2010. Post-eclosion odor  
1024   experience modifies olfactory receptor neuron coding in *Drosophila*. *Proc Natl Acad Sci U*  
1025   *S A* **107**:9855–9860. doi:10.1073/pnas.1003856107
- 1026   Jeanne JM, Wilson RI. 2015. Convergence, Divergence, and Reconvergence in a Feedforward  
1027   Network Improves Neural Speed and Accuracy. *Neuron* **88**:1014–1026.  
1028   doi:10.1016/j.neuron.2015.10.018
- 1029   Johnson W, Turkheimer E, Gottesman II, Bouchard TJ Jr. 2010. Beyond Heritability: Twin  
1030   Studies in Behavioral Research. *Curr Dir Psychol Sci* **18**:217–220. doi:10.1111/j.1467-  
1031   8721.2009.01639.x
- 1032   Kain JS, Stokes C, de Bivort BL. 2012. Phototactic personality in fruit flies and its suppression

- 1033 by serotonin and white. *Proc Natl Acad Sci U S A* **109**:19834–19839.  
1034 doi:10.1073/pnas.1211988109
- 1035 Kain JS, Zhang S, Akhund-Zade J, Samuel ADT, Klein M, de Bivort BL. 2015. Variability in  
1036 thermal and phototactic preferences in *Drosophila* may reflect an adaptive bet-hedging  
1037 strategy. *Evolution* **69**:3171–3185. doi:10.1111/evo.12813
- 1038 Kakaria KS, de Bivort BL. 2017. Ring Attractor Dynamics Emerge from a Spiking Model of the  
1039 Entire Protocerebral Bridge. *Front Behav Neurosci* **11**:8. doi:10.3389/fnbeh.2017.00008
- 1040 Kao K-W, Lo C-C. 2020. Short term depression, presynaptic inhibition and local neuron  
1041 diversity play key functional roles in the insect antennal lobe. *J Comput Neurosci*.  
1042 doi:10.1007/s10827-020-00747-4
- 1043 Kluyver T, Ragan-Kelley B, Pérez F, Granger B, Bussonnier M, Frederic J, Kelley K, Hamrick J,  
1044 Grout J, Corlay S, Ivanov P, Avila D, Abdalla S, Willing C. 2016. Jupyter Notebooks -- a  
1045 publishing format for reproducible computational workflows In: Loizides F, Schmidt B,  
1046 editors. Positioning and Power in Academic Publishing: Players, Agents and Agendas. IOS  
1047 Press. pp. 87–90.
- 1048 Körholz JC, Zocher S, Grzyb AN, Morisse B, Poetzsch A, Ehret F, Schmied C, Kempermann G.  
1049 2018. Selective increases in inter-individual variability in response to environmental  
1050 enrichment in female mice. *eLife* **7**. doi:10.7554/eLife.35690
- 1051 Krams IA, Krama T, Krams R, Trakimas G, Popovs S, Jöers P, Munkevics M, Elferts D, Rantala  
1052 MJ, Makņa J, de Bivort BL. 2021. Serotonergic Modulation of Phototactic Variability  
1053 Underpins a Bet-Hedging Strategy in *Drosophila melanogaster*. *Front Behav Neurosci*  
1054 **15**:659331. doi:10.3389/fnbeh.2021.659331
- 1055 Laskowski KL, Bierbach D, Jolles JW, Doran C, Wolf M. 2022. The emergence and  
1056 development of behavioral individuality in clonal fish. *Nat Commun* **13**:1–9.  
1057 doi:10.1038/s41467-022-34113-y
- 1058 Li H, Horns F, Wu B, Xie Q, Li J, Li T, Luginbuhl DJ, Quake SR, Luo L. 2017. Classifying  
1059 *Drosophila* Olfactory Projection Neuron Subtypes by Single-Cell RNA Sequencing. *Cell*  
1060 **171**:1206–1220.e22. doi:10.1016/j.cell.2017.10.019
- 1061 Linneweber GA, Andriatsilavo M, Dutta SB, Bengochea M, Hellbruegge L, Liu G, Ejsmont RK,  
1062 Straw AD, Wernet M, Hiesinger PR, Hassan BA. 2020. A neurodevelopmental origin of  
1063 behavioral individuality in the *Drosophila* visual system. *Science* **367**:1112–1119.  
1064 doi:10.1126/science.aaw7182
- 1065 Liu TX, Davoudian PA, Lizbinski KM, Jeanne JM. 2022. Connectomic features underlying  
1066 diverse synaptic connection strengths and subcellular computation. *Curr Biol* **32**:559–  
1067 569.e5. doi:10.1016/j.cub.2021.11.056
- 1068 Luo SX, Axel R, Abbott LF. 2010. Generating sparse and selective third-order responses in the  
1069 olfactory system of the fly. *Proc Natl Acad Sci U S A* **107**:10713–10718.  
1070 doi:10.1073/pnas.1005635107
- 1071 Maloney RT. 2021. Neuromodulation and Individuality. *Front Behav Neurosci* **15**:777873.  
1072 doi:10.3389/fnbeh.2021.777873
- 1073 Marder E. 2011. Variability, compensation, and modulation in neurons and circuits. *Proc Natl*  
1074 *Acad Sci U S A* **108 Suppl 3**:15542–15548. doi:10.1073/pnas.1010674108
- 1075 MATLAB pca documentation. n.d. . *MathWorks*.  
1076 <https://www.mathworks.com/help/stats/pca.html>
- 1077 Mazor O, Laurent G. 2005. Transient dynamics versus fixed points in odor representations by  
1078 locust antennal lobe projection neurons. *Neuron* **48**:661–673.

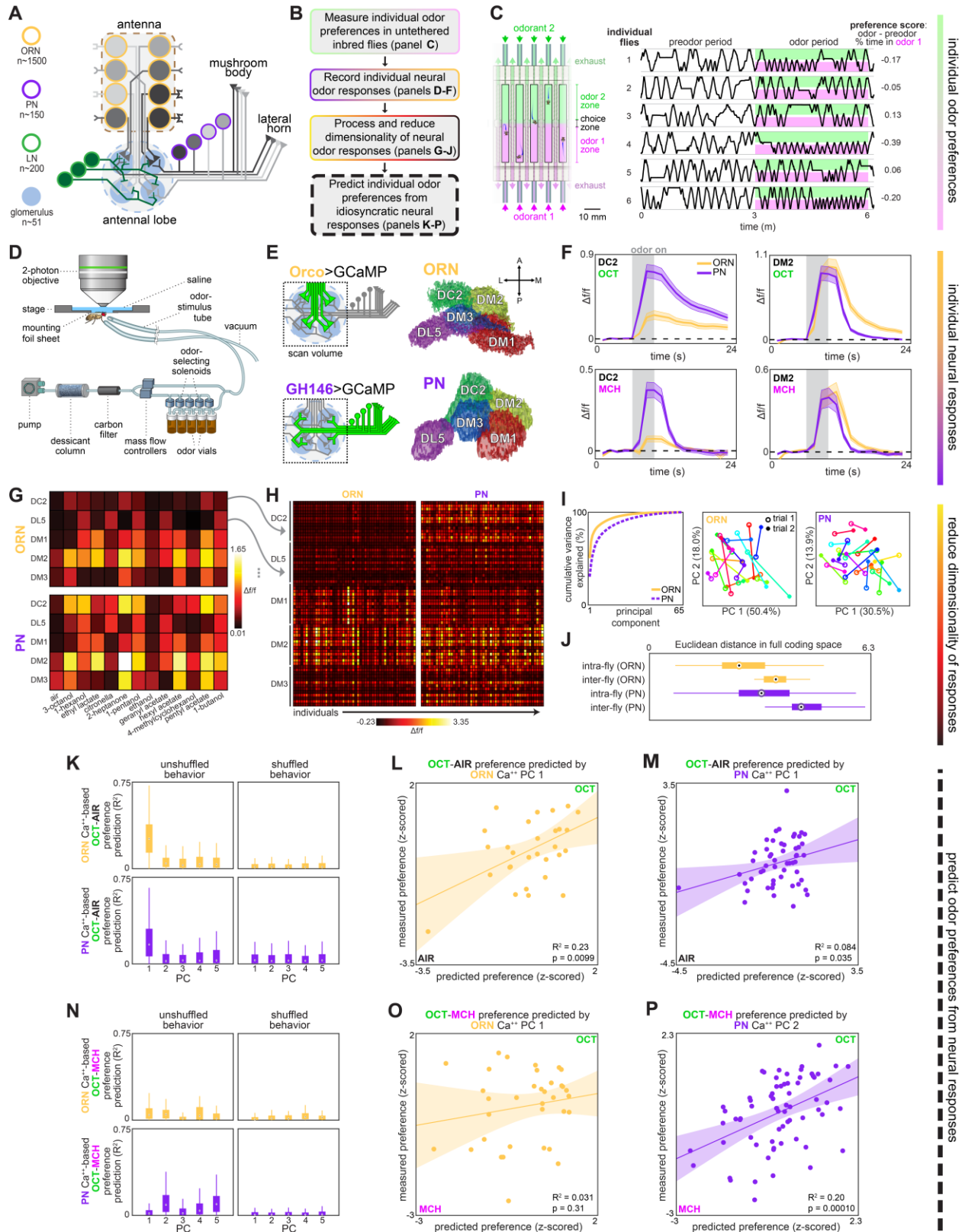
- 1079 doi:10.1016/j.neuron.2005.09.032  
1080 McLaughlin CN, Brbić M, Xie Q, Li T, Horns F, Kolluru SS, Kebschull JM, Vacek D, Xie A, Li  
1081 J, Jones RC, Leskovec J, Quake SR, Luo L, Li H. 2021. Single-cell transcriptomes of  
1082 developing and adult olfactory receptor neurons in *Drosophila*. *eLife* **10**.  
1083 doi:10.7554/eLife.63856  
1084 Mellert DJ, Williamson WR, Shirangi TR, Card GM, Truman JW. 2016. Genetic and  
1085 Environmental Control of Neurodevelopmental Robustness in *Drosophila*. *PLoS One*  
1086 **11**:e0155957. doi:10.1371/journal.pone.0155957  
1087 Michelson CA, Pillow JW, Seidemann E. 2017. Majority of choice-related variability in  
1088 perceptual decisions is present in early sensory cortex. *bioRxiv*. doi:10.1101/207357  
1089 Mosca TJ, Luo L. 2014. Synaptic organization of the *Drosophila* antennal lobe and its regulation  
1090 by the Teneurins. *eLife*. doi:10.7554/elife.03726  
1091 Münch D, Galizia CG. 2016. DoOR 2.0--Comprehensive Mapping of *Drosophila melanogaster*  
1092 Odorant Responses. *Sci Rep* **6**:21841. doi:10.1038/srep21841  
1093 Nagel KI, Hong EJ, Wilson RI. 2015. Synaptic and circuit mechanisms promoting broadband  
1094 transmission of olfactory stimulus dynamics. *Nat Neurosci* **18**:56–65. doi:10.1038/nn.3895  
1095 Newsome WT, Britten KH, Anthony Movshon J. 1989. Neuronal correlates of a perceptual  
1096 decision. *Nature*. doi:10.1038/341052a0  
1097 Olsen SR, Wilson RI. 2008. Lateral presynaptic inhibition mediates gain control in an olfactory  
1098 circuit. *Nature* **452**:956–960. doi:10.1038/nature06864  
1099 Osborne LC, Lisberger SG, Bialek W. 2005. A sensory source for motor variation. *Nature*  
1100 **437**:412–416. doi:10.1038/nature03961  
1101 Pisokas I, Heinze S, Webb B. 2020. The head direction circuit of two insect species. *eLife* **9**.  
1102 doi:10.7554/eLife.53985  
1103 Raj A, Rifkin SA, Andersen E, van Oudenaarden A. 2010. Variability in gene expression  
1104 underlies incomplete penetrance. *Nature* **463**:913–918. doi:10.1038/nature08781  
1105 Rihani K, Sachse S. 2022. Shedding Light on Inter-Individual Variability of Olfactory Circuits in  
1106 *Drosophila*. *Front Behav Neurosci* **16**. doi:10.3389/fnbeh.2022.835680  
1107 Rohatgi A. 2021. Webplotdigitizer: Version 4.5.  
1108 Sachse S, Rueckert E, Keller A, Okada R, Tanaka NK, Ito K, Vosshall LB. 2007. Activity-  
1109 dependent plasticity in an olfactory circuit. *Neuron* **56**:838–850.  
1110 doi:10.1016/j.neuron.2007.10.035  
1111 Scheffer LK, Xu CS, Januszewski M, Lu Z, Takemura S-Y, Hayworth KJ, Huang GB,  
1112 Shinomiya K, Maitlin-Shepard J, Berg S, Clements J, Hubbard PM, Katz WT, Umayam L,  
1113 Zhao T, Ackerman D, Blakely T, Bogovic J, Dolafi T, Kainmueller D, Kawase T, Khairy  
1114 KA, Leavitt L, Li PH, Lindsey L, Neubarth N, Olbris DJ, Otsuna H, Trautman ET, Ito M,  
1115 Bates AS, Goldammer J, Wolff T, Svirskas R, Schlegel P, Neace E, Knecht CJ, Alvarado  
1116 CX, Bailey DA, Ballinger S, Borycz JA, Canino BS, Cheatham N, Cook M, Dreher M,  
1117 Duclos O, Eubanks B, Fairbanks K, Finley S, Forknall N, Francis A, Hopkins GP, Joyce  
1118 EM, Kim S, Kirk NA, Kovalyak J, Lauchie SA, Lohff A, Maldonado C, Manley EA, McLin  
1119 S, Mooney C, Ndama M, Ogundeyi O, Okeoma N, Ordish C, Padilla N, Patrick CM,  
1120 Paterson T, Phillips EE, Phillips EM, Rampally N, Ribeiro C, Robertson MK, Rymer JT,  
1121 Ryan SM, Sammons M, Scott AK, Scott AL, Shinomiya A, Smith C, Smith K, Smith NL,  
1122 Sobeski MA, Suleiman A, Swift J, Takemura S, Talebi I, Tarnogorska D, Tenshaw E, Tokhi  
1123 T, Walsh JJ, Yang T, Horne JA, Li F, Parekh R, Rivlin PK, Jayaraman V, Costa M, Jefferis  
1124 GS, Ito K, Saalfeld S, George R, Meinertzhagen IA, Rubin GM, Hess HF, Jain V, Plaza

- 1125 SM. 2020. A connectome and analysis of the adult *Drosophila* central brain. *eLife* **9**.  
1126 doi:10.7554/eLife.57443
- 1127 Schlegel P, Bates AS, Stürner T, Jagannathan S, Drummond N, Hsu J, Capdevila LS, Javier A,  
1128 Marin EC, Barth-Maron A, Tamimi IFM, Li F, Rubin GM, Plaza SM, Costa M, Jefferis  
1129 GSXE. 2020. Information flow, cell types and stereotypy in a full olfactory connectome.  
1130 *bioRxiv*. doi:10.1101/2020.12.15.401257
- 1131 Schuett W, Dall SRX, Baeumer J, Kloesener MH, Nakagawa S, Beinlich F, Eggers T. 2011.  
1132 Personality variation in a clonal insect: the pea aphid, *Acyrtosiphon pisum*. *Dev*  
1133 *Psychobiol* **53**:631–640. doi:10.1002/dev.20538
- 1134 Seki Y, Rybak J, Wicher D, Sachse S, Hansson BS. 2010. Physiological and morphological  
1135 characterization of local interneurons in the *Drosophila* antennal lobe. *J Neurophysiol*  
1136 **104**:1007–1019. doi:10.1152/jn.00249.2010
- 1137 Shang Y, Claridge-Chang A, Sjulson L, Pypaert M, Miesenböck G. 2007. Excitatory local  
1138 circuits and their implications for olfactory processing in the fly antennal lobe. *Cell*  
1139 **128**:601–612. doi:10.1016/j.cell.2006.12.034
- 1140 Sizemore TR, Dacks AM. 2016. Serotonergic Modulation Differentially Targets Distinct  
1141 Network Elements within the Antennal Lobe of *Drosophila melanogaster*. *Sci Rep* **6**:37119.  
1142 doi:10.1038/srep37119
- 1143 Skutt-Kakaria K, Reimers P, Currier TA, Werkhoven Z, de Bivort BL. 2019. A neural circuit  
1144 basis for context-modulation of individual locomotor behavior. *bioRxiv*.  
1145 doi:10.1101/797126
- 1146 Stern S, Kirst C, Bargmann CI. 2017. Neuromodulatory Control of Long-Term Behavioral  
1147 Patterns and Individuality across Development. *Cell* **171**:1649–1662.e10.  
1148 doi:10.1016/j.cell.2017.10.041
- 1149 Tobin WF, Wilson RI, Lee W-CA. 2017. Wiring variations that enable and constrain neural  
1150 computation in a sensory microcircuit. *eLife* **6**:e24838. doi:10.7554/eLife.24838
- 1151 Tsai K-T, Hu C-K, Li K-W, Hwang W-L, Chou Y-H. 2018. Circuit variability interacts with  
1152 excitatory-inhibitory diversity of interneurons to regulate network encoding capacity. *Sci*  
1153 *Rep* **8**:8027. doi:10.1038/s41598-018-26286-8
- 1154 van Rossum G, Drake FL. 2011. The Python Language Reference Manual. Network Theory Ltd.  
1155 Werkhoven Z, Bravin A, Skutt-Kakaria K, Reimers P, Pallares LF, Ayroles J, de Bivort BL.  
1156 2021. The structure of behavioral variation within a genotype. *eLife* **10**:e64988.  
1157 doi:10.7554/eLife.64988
- 1158 Wilson RI. 2013. Early Olfactory Processing in *Drosophila*: Mechanisms and Principles. *Annual*  
1159 *Review of Neuroscience*. doi:10.1146/annurev-neuro-062111-150533
- 1160 Wilson RI. 2004. Transformation of Olfactory Representations in the *Drosophila* Antennal Lobe.  
1161 *Science*. doi:10.1126/science.1090782
- 1162 Wilson RI, Laurent G. 2005. Role of GABAergic inhibition in shaping odor-evoked  
1163 spatiotemporal patterns in the *Drosophila* antennal lobe. *J Neurosci* **25**:9069–9079.  
1164 doi:10.1523/JNEUROSCI.2070-05.2005
- 1165 Wilson RI, Turner GC, Laurent G. 2004. Transformation of olfactory representations in the  
1166 *Drosophila* antennal lobe. *Science* **303**:366–370. doi:10.1126/science.1090782
- 1167 Wu JS, Luo L. 2006. A protocol for dissecting *Drosophila melanogaster* brains for live imaging  
1168 or immunostaining. *Nat Protoc* **1**:2110–2115. doi:10.1038/nprot.2006.336
- 1169 Xie Q, Brbic M, Horns F, Kolluru SS, Jones RC, Li J, Reddy AR, Xie A, Kohani S, Li Z,  
1170 McLaughlin CN, Li T, Xu C, Vacek D, Luginbuhl DJ, Leskovec J, Quake SR, Luo L, Li H.

- 1171            2021. Temporal evolution of single-cell transcriptomes of *Drosophila* olfactory projection  
1172            neurons. *eLife* **10**. doi:10.7554/eLife.63450  
1173        Yaksi E, Wilson RI. 2010. Electrical coupling between olfactory glomeruli. *Neuron* **67**:1034–  
1174            1047. doi:10.1016/j.neuron.2010.08.041  
1175        Zocher S, Schilling S, Grzyb AN, Adusumilli VS, Bogado Lopes J, Günther S, Overall RW,  
1176            Winter Y, Kempermann G. 2020. Early-life environmental enrichment generates persistent  
1177            individualized behavior in mice. *Sci Adv* **6**:eabb1478. doi:10.1126/sciadv.abb1478

## 1178 **Figures and figure supplements**





1179

1180

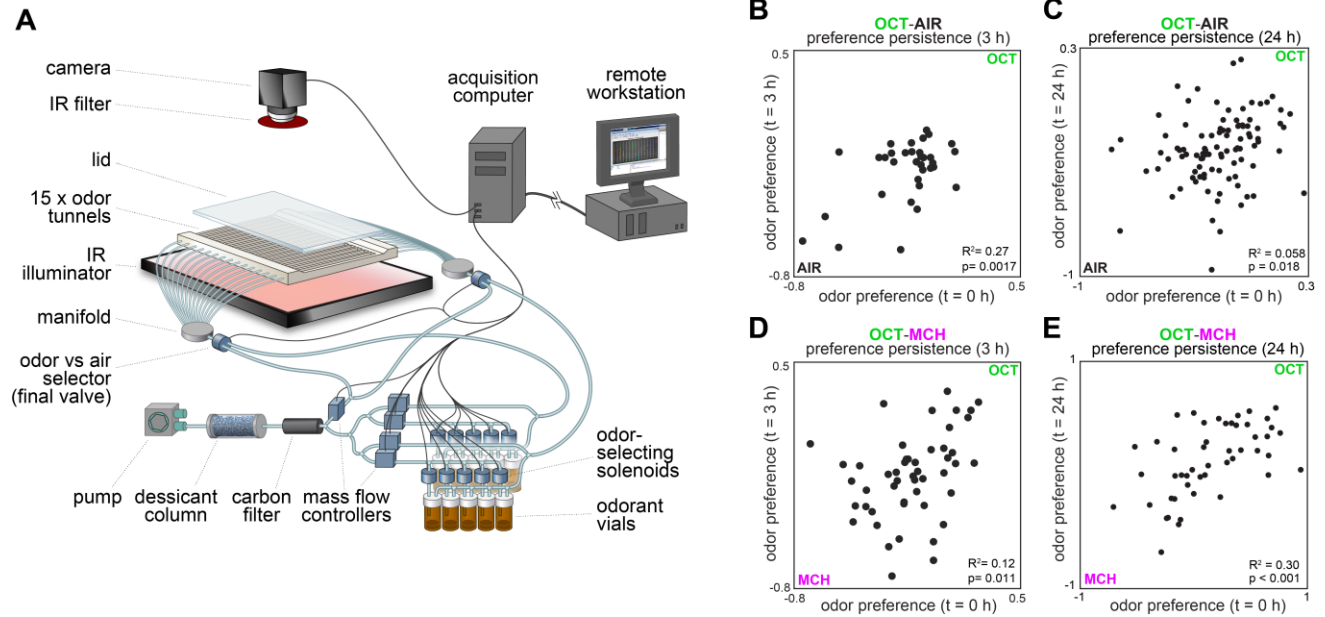
1181

1182

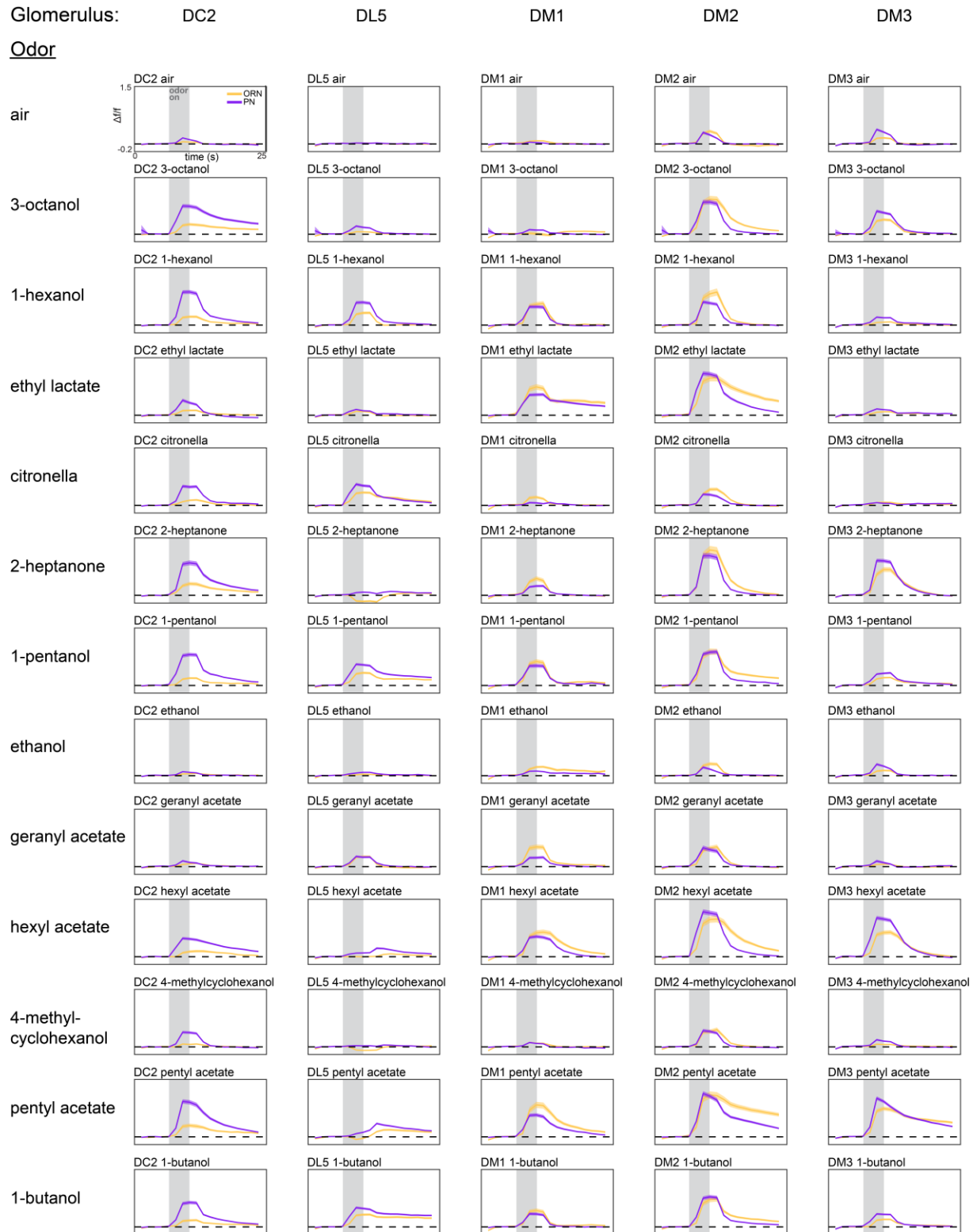
**Figure 1. Idiosyncratic calcium dynamics predict individual odor preferences.**

(A) Olfactory circuit schematic. Olfactory receptor neurons (ORNs, peach outline) and projection neurons (PNs, plum outline) are comprised of ~51 classes corresponding to odor

1183 receptor response channels. ORNs (gray shading) sense odors in the antennae and synapse on  
1184 dendrites of PNs of the same class in ball-shaped structures called glomeruli located in the  
1185 antennal lobe (AL). Local neurons (LNs, green outline) mediate interglomerular cross-talk and  
1186 presynaptic inhibition, amongst other roles (Olsen and Wilson, 2008; Yaksi and Wilson, 2010).  
1187 Odor signals are normalized and whitened in the AL before being sent to the mushroom body  
1188 and lateral horn for further processing. Schematic adapted from Honegger et al., 2019 **(B)**  
1189 Experiment outline. **(C)** Odor preference behavior tracking setup (reproduced from Honegger,  
1190 Smith, et al. (Honegger et al., 2019)) and example individual fly ethograms. OCT (green) and  
1191 MCH (magenta) were presented for 3 minutes. **(D)** Head-fixed 2-photon calcium imaging and  
1192 odor delivery setup (reproduced from Honegger et al., 2019) **(E)** Orco and GH146 driver  
1193 expression profiles (left) and example segmentation masks (right) extracted from 2-photon  
1194 calcium images for a single fly expressing Orco>GCaMP6m (top, expressed in a subset of all  
1195 ORN classes) or GH146>Gcamp6m (bottom, expressed in a subset of all PN classes). **(F)** Time-  
1196 dependent  $\Delta f/f$  for glomerular odor responses in ORNs (peach) and PNs (plum) averaged across  
1197 all individuals: DC2 to OCT (upper left), DM2 to OCT (upper right), DC2 to MCH (lower left),  
1198 and DM2 to OCT (lower right). Shaded error bars represent S.E.M. **(G)** Peak  $\Delta f/f$  for each  
1199 glomerulus-odor pair averaged across all flies. **(H)** Individual neural responses measured in  
1200 ORNs (left) or PNs (right) for 50 flies each. Columns represent the average of up to 4 odor  
1201 responses from a single fly. Each row represents one glomerulus-odor response pair. Odors are  
1202 the same as in panel (G). **(I)** Principal component analysis of individual neural responses.  
1203 Fraction of variance explained versus principal component number (left). Trial 1 and trial 2 of  
1204 ORN (middle) and PN (right) responses for 20 individuals (unique colors) embedded in PC 1-2  
1205 space. **(J)** Euclidean distances between glomerulus-odor responses within and across flies  
1206 measured in ORNs (n=65 flies) and PNs (n=122 flies). Distances calculated without PCA  
1207 compression. Points represent the median value, boxes represent the interquartile range, and  
1208 whiskers the range of the data. **(K)** Bootstrapped  $R^2$  of OCT-AIR preference prediction from  
1209 each of the first 5 principal components of neural activity measured in ORNs (top, all data) or  
1210 PNs (bottom, training set). **(L)** Measured OCT-AIR preference versus preference predicted from  
1211 PC 1 of ORN activity (n=30 flies). **(M)** Measured OCT-AIR preference versus preference  
1212 predicted from PC 1 of PN activity in n=53 flies using a model trained on a training set of n=18  
1213 flies (see Figure 2 – figure supplement 1A-B for train/test flies analyzed separately). **(N)**  
1214 Bootstrapped  $R^2$  of OCT-MCH preference prediction from each of the first 5 principal  
1215 components of neural activity measured in ORNs (top, all data) or PNs (bottom, training set).  
1216 **(O)** Measured OCT-MCH preference versus preference predicted from PC 1 of ORN activity  
1217 (n=35 flies). **(P)** Measured OCT-MCH preference versus preference predicted from PC 2 of PN  
1218 activity in n=69 flies using a model trained on a training set of n=47 flies (see Figure 2 – figure  
1219 supplement 1C-D for train/test flies analyzed separately). Shaded regions in L,M,O,P are the  
1220 95% CI of the fit estimated by bootstrapping.

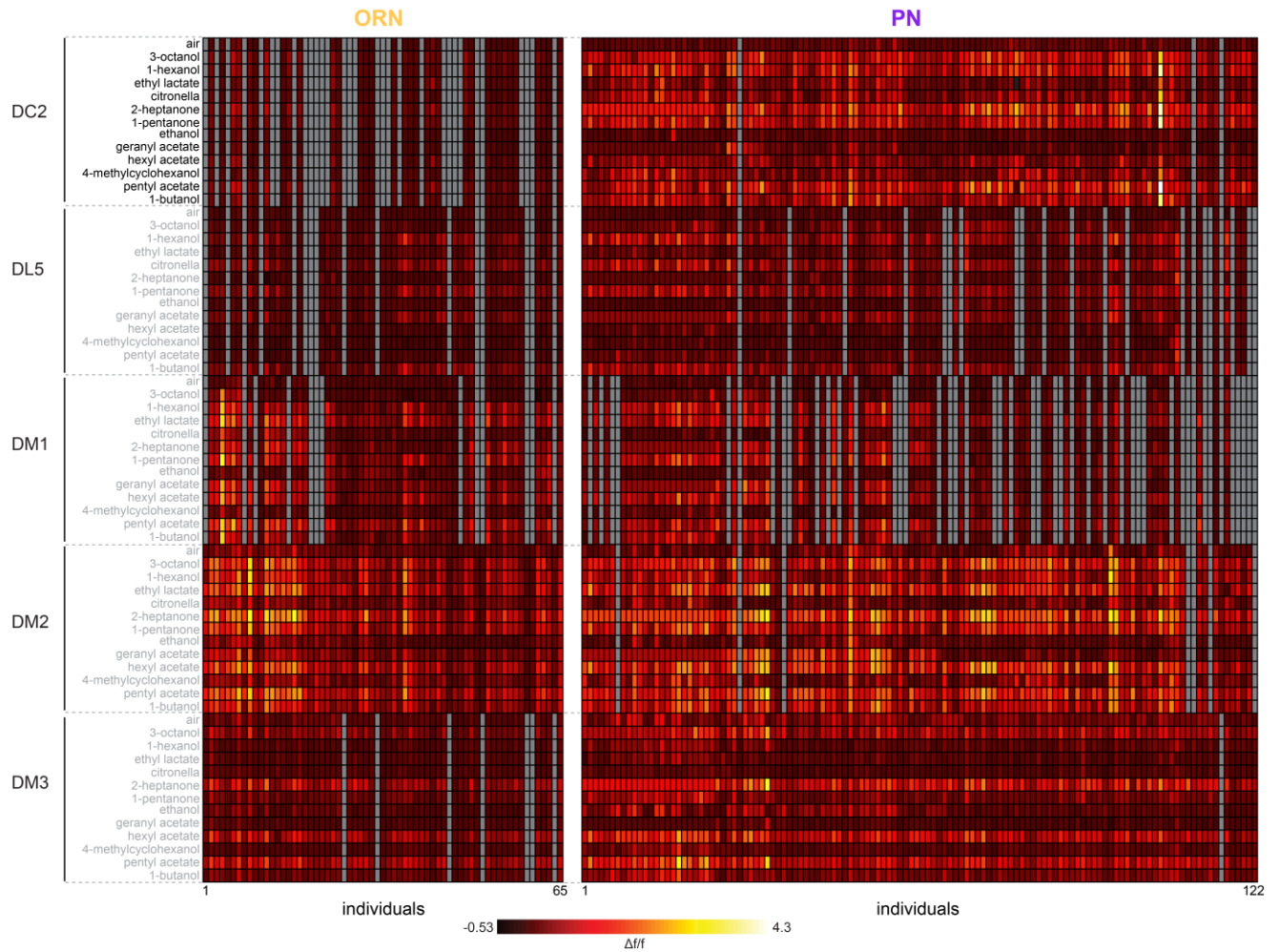


1221  
1222 **Figure 1 – figure supplement 1. Behavioral measurements and individual preference**  
1223 **persistence.**  
1224 **(A)** Behavioral measurement apparatus (adapted from Honegger et al., 2019) **(B)** Odor  
1225 preference persistence over 3 hours for flies given a choice between 3-octanol and air (n=34  
1226 flies). **(C)** Odor preference persistence over 24 hours for flies given a choice between 3-octanol  
1227 and air (n=97 flies). **(D)** Odor preference persistence over 3 hours for flies given a choice  
1228 between 3-octanol and 4-methylcyclohexanol (n=51 flies). **(E)** Odor preference persistence over  
1229 24 hours for flies given a choice between 3-octanol and 4-methylcyclohexanol (n=49 flies).



1230  
1231  
1232  
1233  
1234

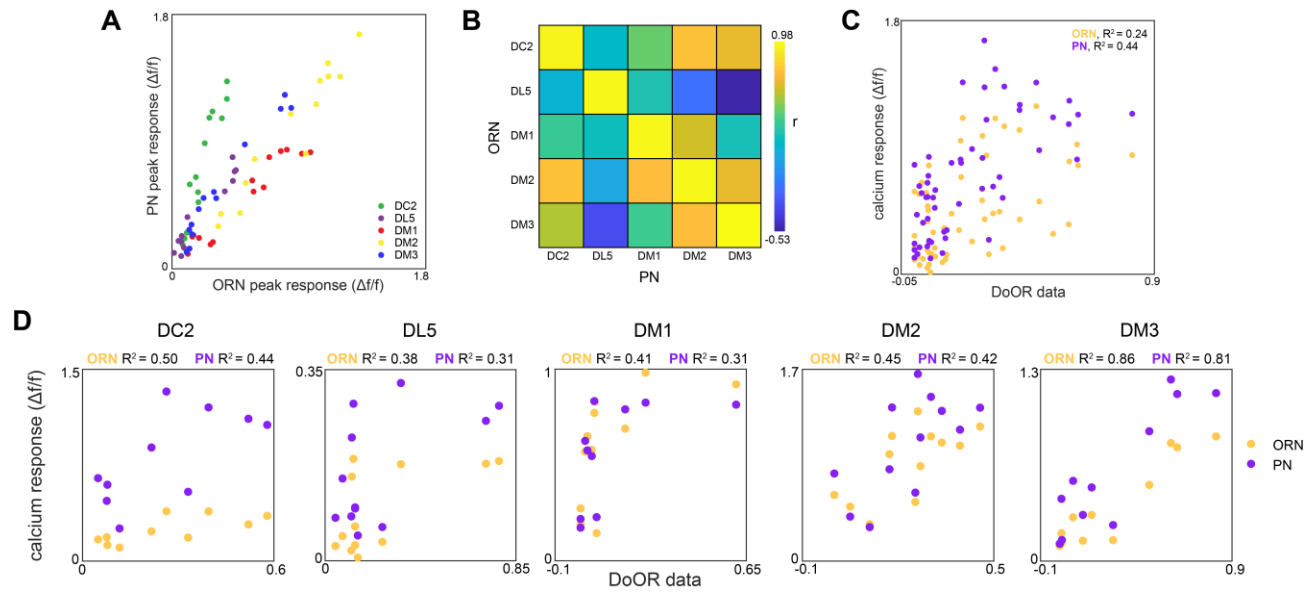
**Figure 1 – figure supplement 2. Average glomerulus-odor time-dependent responses.** Time-dependent responses of each glomerulus identified in our study to the 13 odors in our odor panel. Data represents the average across flies (ORN, peach curves, n=65 flies; PN, plum curves, n=122 flies). Shaded error bars represent S.E.M.



1235  
1236  
1237  
1238  
1239  
1240

**Figure 1 – figure supplement 3. Individual glomerulus-odor responses.**

Idiosyncratic odor coding measured in ORNs (left, n=65 flies) and PNs (right, n=122 flies). Each column represents the response (max  $\Delta f/f$  attained over the odor trial) of a single fly averaged over up to 4 odor deliveries. Each row represents a glomerulus-odor response pair. Missing data are indicated in gray.

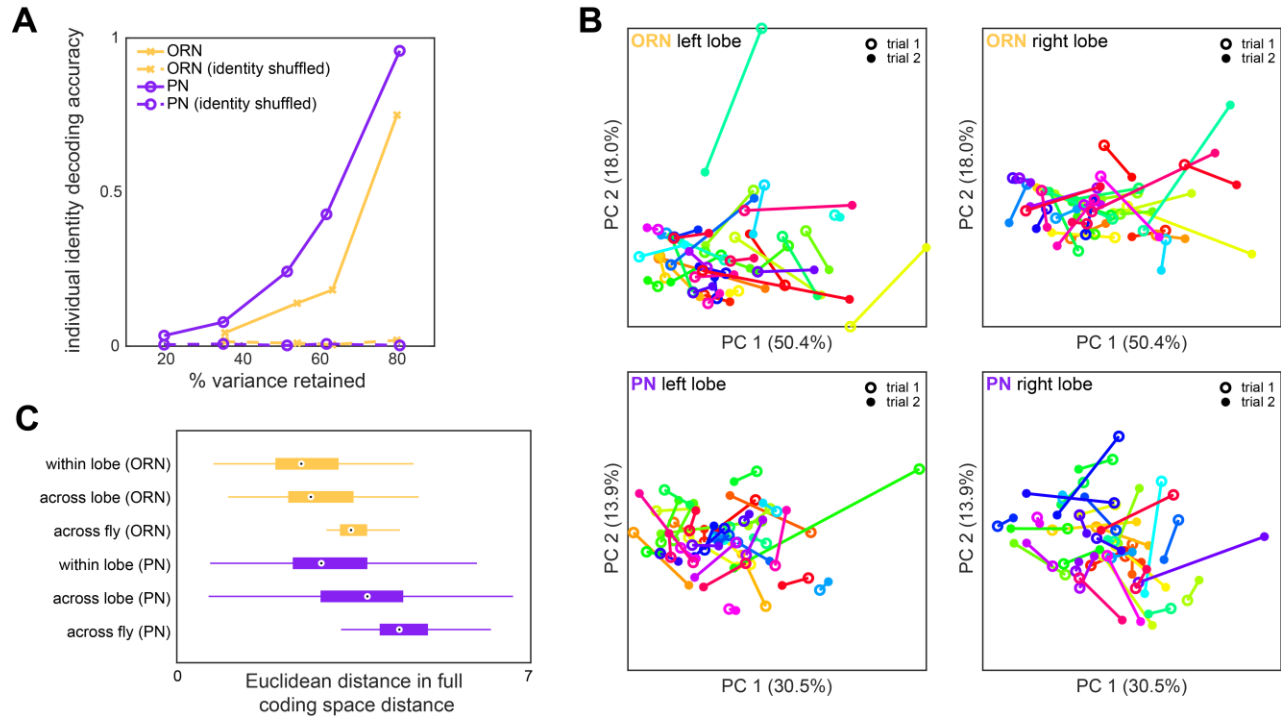


1241  
1242  
1243  
1244  
1245  
1246  
1247  
1248

**Figure 1 – figure supplement 4. Glomerulus responses and identification.**

(A) Glomerulus odor responses measured in PNs versus those measured in ORNs. Points correspond to the odorants listed in Figure 1G. (B) Cross-odor trial correlation matrix between glomerular odor responses in ORNs and PNs. (C) Peak calcium responses for each glomerulus-odor pair measured in this study plotted against those recorded in the DoOR dataset (Münch and Galizia, 2016). (D) Peak calcium responses for each individual glomerulus plotted against those recorded in the DoOR dataset.





1249

1250

**Figure 1 – figure supplement 5. Idiosyncrasy of ORN and PN responses.**

1251

(A) Logistic regression classifier accuracy of decoding individual identity from individual odor panel peak responses. PCA was performed on population responses and the specified fraction of variance (x-axis) was retained. Individual identity can be better decoded from PN responses than ORN responses in all cases. (B) Individual trial-to-trial glomerulus-odor responses embedded in PC 1-2 space. Responses for the same flies as Figure 1I are shown. Each linked color represents one fly. Trial 1 and trial 2 responses are shown for ORN left lobe (upper left), ORN right lobe (upper right), PN left lobe (lower left), and PN right lobe (lower right). (C) Distance in the full glomerulus-odor response space between recordings within a lobe (trial-to-trial), across lobes (within fly), and across flies for ORNs and PNs. Points represent the median value, boxes represent the interquartile range, and whiskers the range of the data.

1252

1253

1254

1255

1256

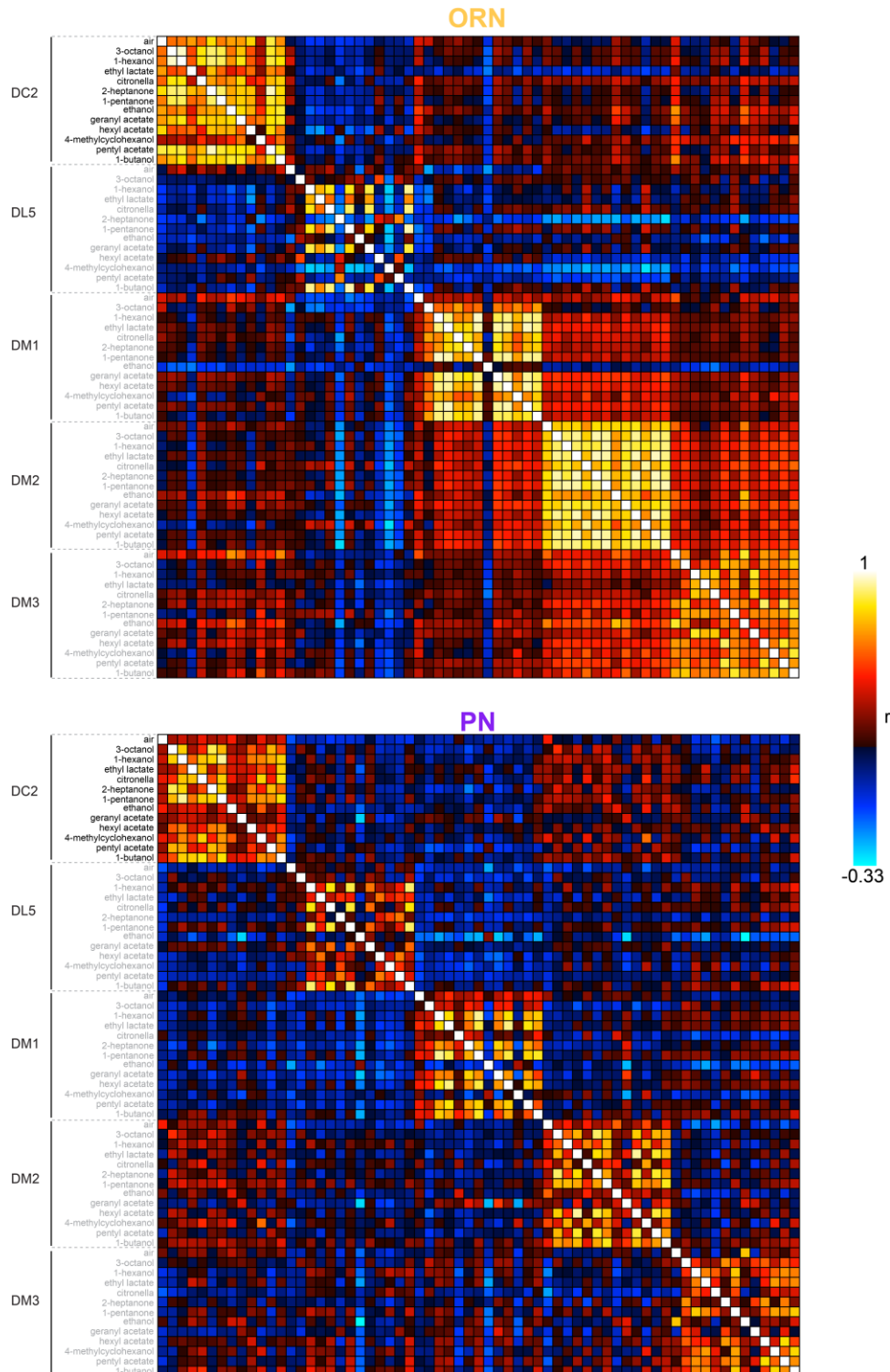
1257

1258

1259

1260

1261



1262

1263

1264

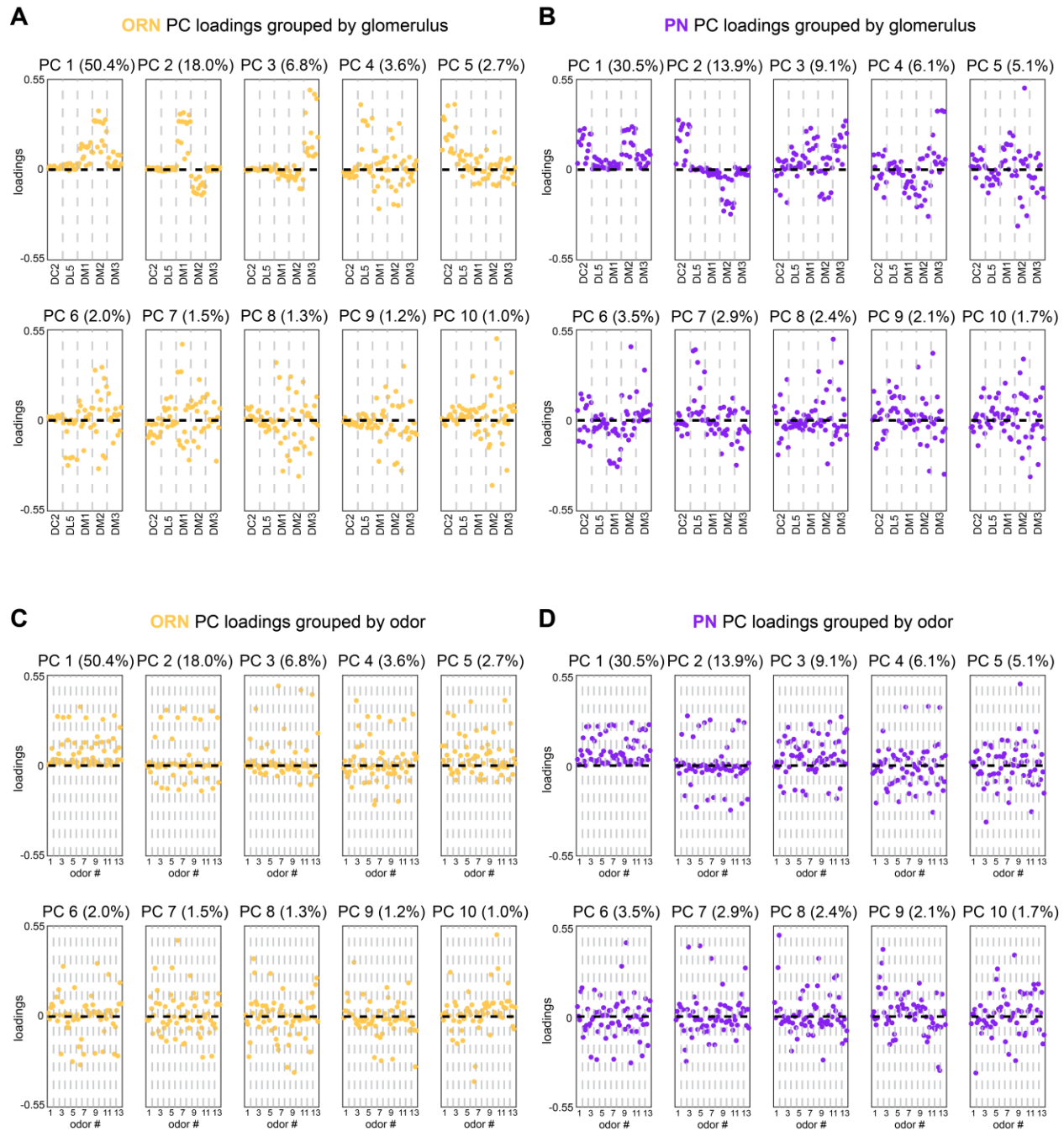
1265

1266

1267

**Figure 1 – figure supplement 6. Calcium response correlation matrices.**

Correlation between calcium response dimensions across flies measured in ORNs (top) and PNs (bottom). Glomerulus-odor responses are correlated at the level of glomeruli in both cell types. Inter-glomerulus correlations are more prominent in ORNs than PNs, consistent with known AL transformations that result in decorrelated PN activity (Bhandawat et al., 2007; Luo et al., 2010).



1268

1269

1270

1271

1272

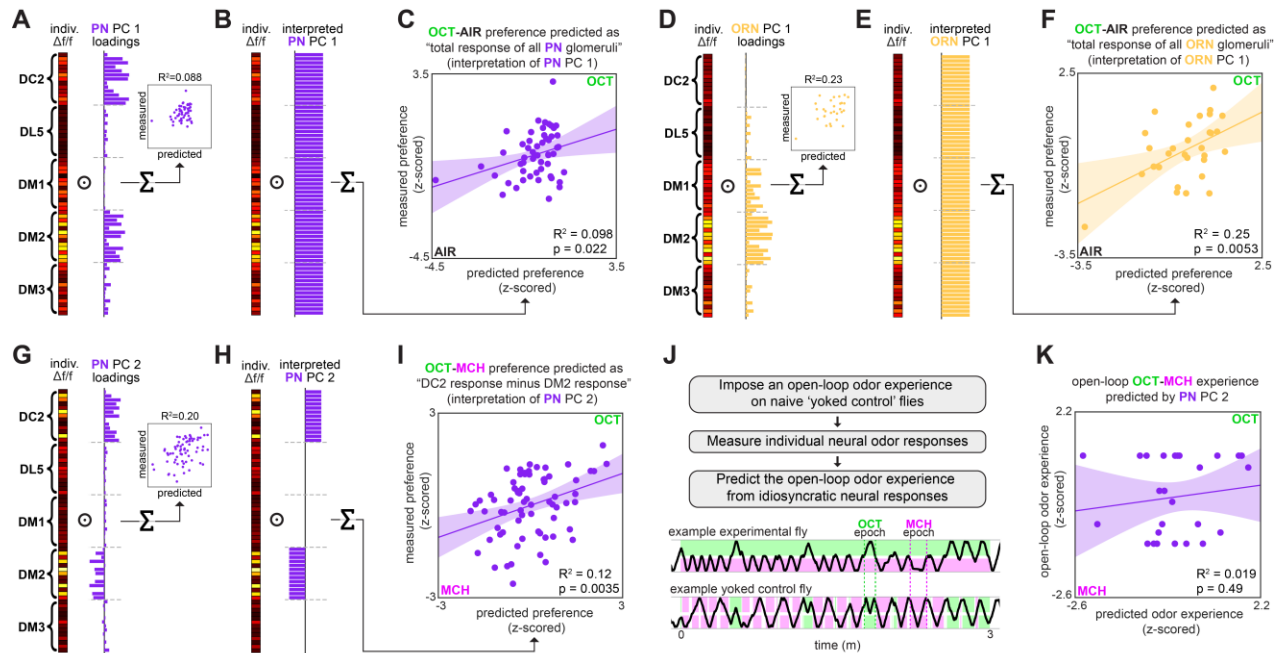
1273

1274

1275

**Figure 1 – figure supplement 7. Calcium imaging principal component loadings.**

(A-B) First 10 principal component loadings measured from calcium responses in ORNs (A, n=65 flies) and PN (B, n=122 flies). Loadings are grouped by glomerulus, with each loading within a glomerulus representing the response of that glomerulus to one odor in the odor panel. Odors are the same as those listed in Figure 1G. (C-D) The same 10 principal component loadings as those shown in panels (A-B) grouped by odor rather than glomerulus. Glomeruli within each odor block are given in the order of panels (A) and (B).



1276

1277

**Figure 2. Variation in global and relative glomerular responses explains individual preferences.**

1278

1279

1280

1281

1282

1283

1284

1285

1286

1287

1288

1289

1290

1291

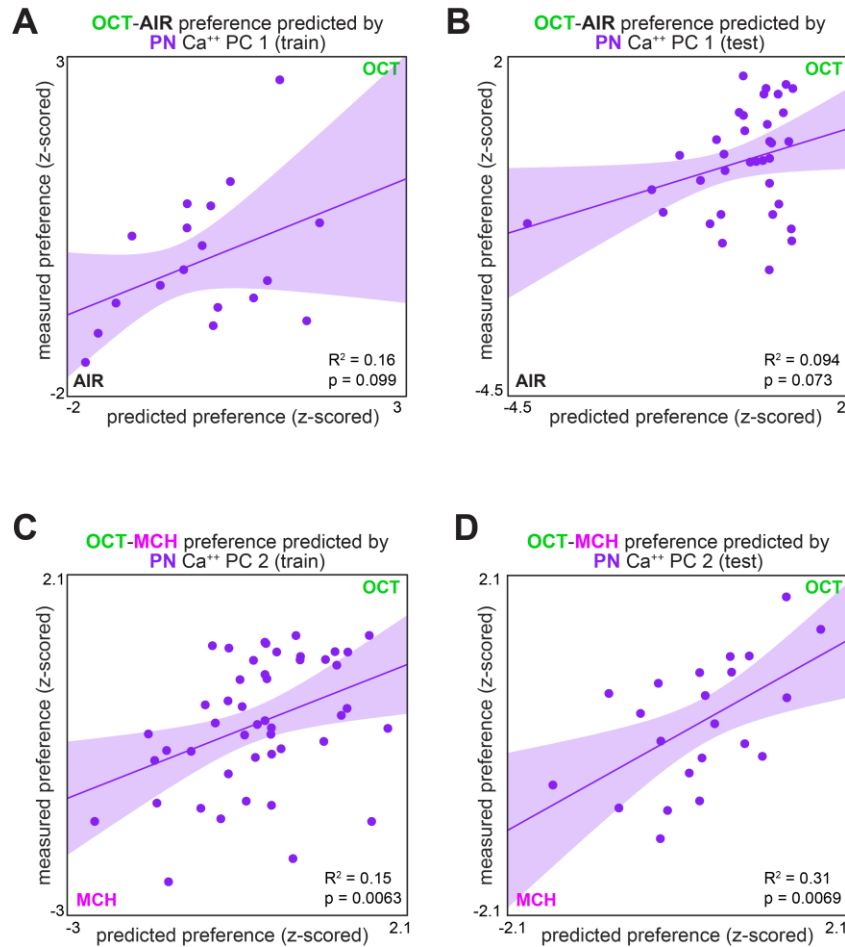
1292

1293

1294

(A) PC 1 loadings of PN activity for flies tested for OCT-AIR preference (n=53 flies). (B) Interpreted PN PC 1 loadings. (C) Measured OCT-AIR preference versus preference predicted by the average peak response across all PN coding dimensions (n=53 flies). (D) PC 1 loadings of ORN activity for flies tested for OCT-AIR preference (n=30 flies). (E) Interpreted ORN PC 1 loadings. (F) Measured OCT-AIR preference versus preference predicted by the average peak response across all ORN coding dimensions (n=30 flies). (G) PC 2 loadings of PN activity for flies tested for OCT-MCH preference (n=69 flies). (H) Interpreted PN PC 2 loadings. (I) Measured OCT-MCH preference versus preference predicted by the average peak PN response in DM2 minus DC2 across all odors (n=69 flies). (J) Yoked control experiment outline and example behavior traces. Experimental flies are free to move about tunnels permeated with steady state OCT and MCH flowing into either end. Yoked control flies are delivered the same odor at both ends of the tunnel which matches the odor experienced at the nose of the experimental fly at each moment in time. (K) Imposed odor experience versus the odor experience predicted from PC 2 of PN activity (n=27 flies) evaluated on the model trained from data in Figure 1P. Shaded regions in C,F,I,K are the 95% CI of the fit estimated by bootstrapping.

1295



1296

1297

1298

1299

1300

1301

1302

1303

1304

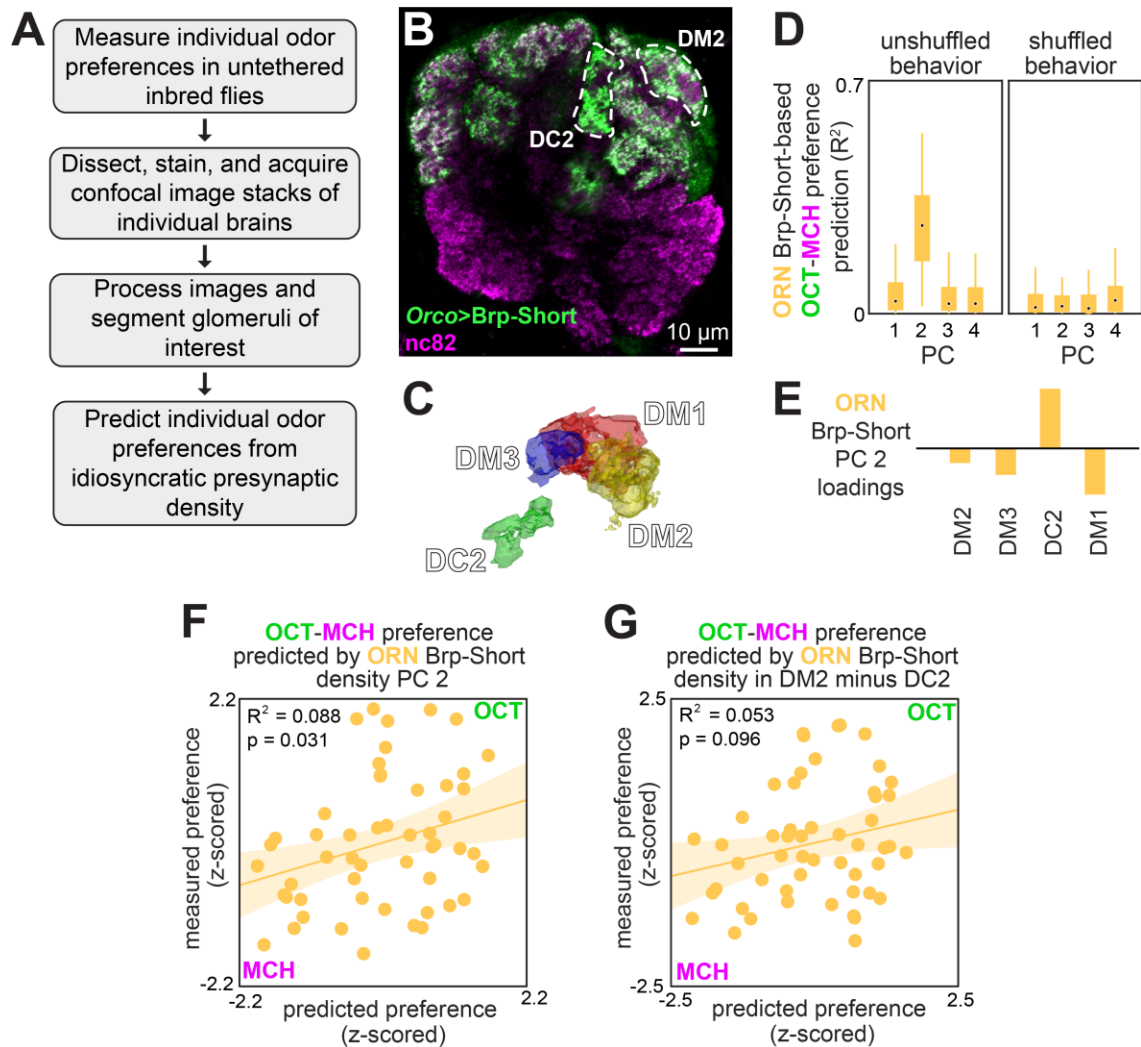
1305

**Figure 2 – figure supplement 1. Measured preference vs. PN activity-based predicted preference, split by training/testing set.**

(A) Measured OCT-AIR preference versus preference predicted from PC 1 of PN activity in a training set (n=18 flies). (B) Measured OCT-AIR preference versus preference predicted from PC 1 on PN activity in a test set (n=35 flies) evaluated on a model trained on data from panel (A). (C) Measured OCT-MCH preference versus preference predicted from PC 2 of PN activity in a training set (n=47 flies). (D) Measured OCT-MCH preference versus preference predicted from PC 2 on PN activity in a test set (n=22 flies) evaluated on a model trained on data from panel (C).



1306



1307

1308

1309

1310

1311

1312

1313

1314

1315

1316

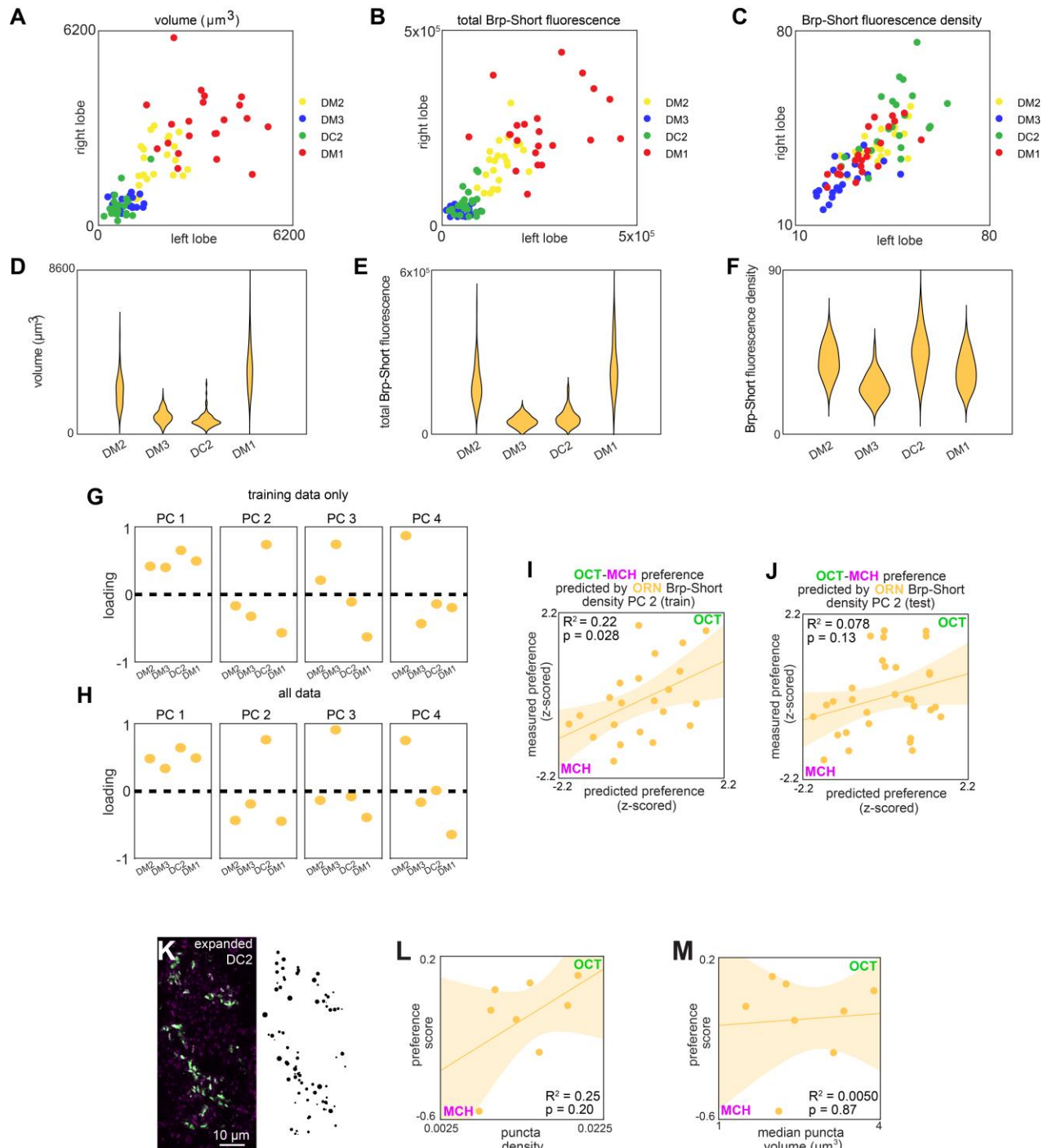
1317

1318

1319

**Figure 3. Idiosyncratic presynaptic marker density in DM2 and DC2 predicts OCT-MCH preference.**

(A) Experiment outline. (B) Example slice from a z-stack of the antennal lobe expressing Orco>Brp-Short (green) with DC2 and DM2 visible (white dashed outline). nc82 counterstain (magenta). (C) Example glomerulus segmentation masks extracted from an individual z-stack. (D) Bootstrapped  $R^2$  of OCT-MCH preference prediction from each of the first 4 principal components of Brp-Short density measured in ORNs (training set,  $n=22$  flies). (E) PC 2 loadings of Brp-Short density. (F) Measured OCT-MCH preference versus preference predicted from PC 2 of ORN Brp-Short density in  $n=53$  flies using a model trained on a training set of  $n=22$  flies (see Figure 3 – figure supplement 1 for train/test flies analyzed separately). (G) Measured OCT-MCH preference versus preference predicted from ORN Brp-Short density in DM2 minus DC2 ( $n=53$  flies).

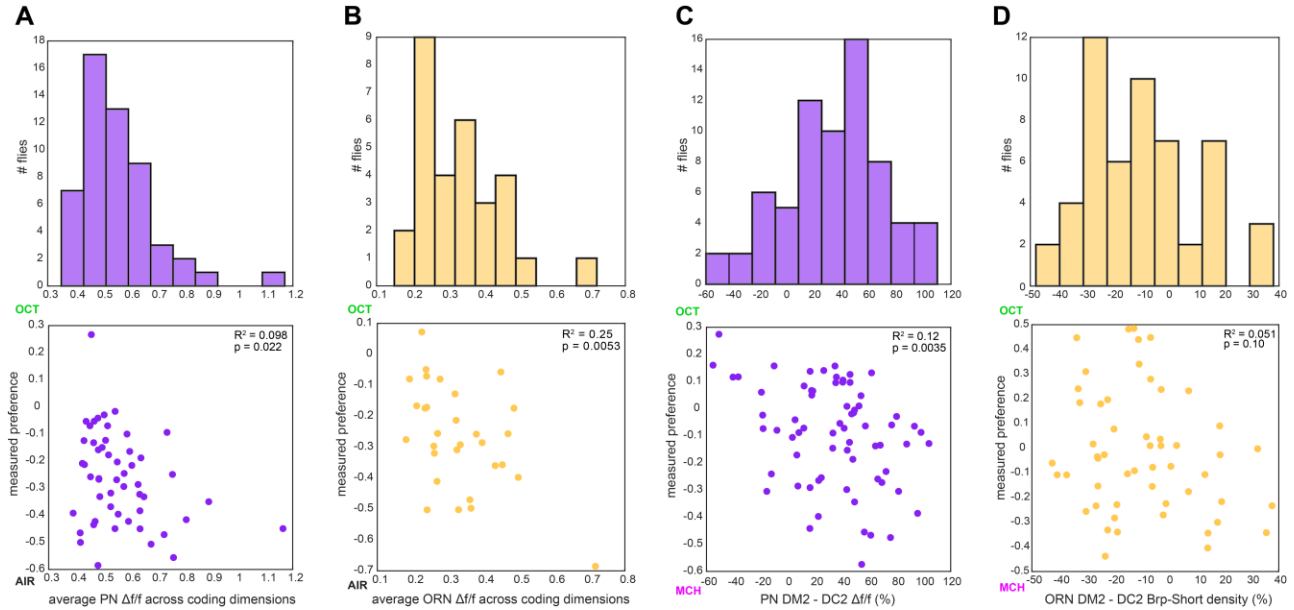


1320  
1321  
1322  
1323  
1324  
1325  
1326  
1327  
1328

**Figure 3 – figure supplement 1. ORN>Brp-Short characterization and model predictions.**

(A-C) Right versus left glomerulus properties measured from z-stacks of stained Orco>Brp-Short samples: (A) Volume, (B) total Brp-Short fluorescence, (C) Brp-Short fluorescence density. (D-F) Same data as panels (A-C) represented in violin plots (kernel density estimated). (G) Principal component loadings of Brp-Short density calculated using only training data (n=22 flies). (H) Principal component loadings of Brp-Short density calculated using all data (n=53 flies). (I) Measured OCT-MCH preference versus preference predicted from PC 2 of ORN Brp-Short density in a training set (n=22 flies). (J) Measured OCT-MCH preference versus

1329 preference predicted from PC 2 on ORN Brp-Short density in a test set (n=31 flies) evaluated on  
1330 a model trained on data from panel (I). **(K)** Example expanded AL expressing Or13a>Brp-Short  
1331 (left) and Imaris-identified puncta from that sample (right). **(L)** OCT-MCH preference score  
1332 plotted against Brp-Short puncta density in expanded Or13a>Brp-Short samples (n=8 flies). **(M)**  
1333 OCT-MCH preference score plotted against Brp-Short median puncta volume in expanded  
1334 Or13a>Brp-Short samples (n=8 flies). Shaded regions in F,G,I,J are the 95% CI of the fit  
1335 estimated by bootstrapping.



1336

1337

1338

1339

1340

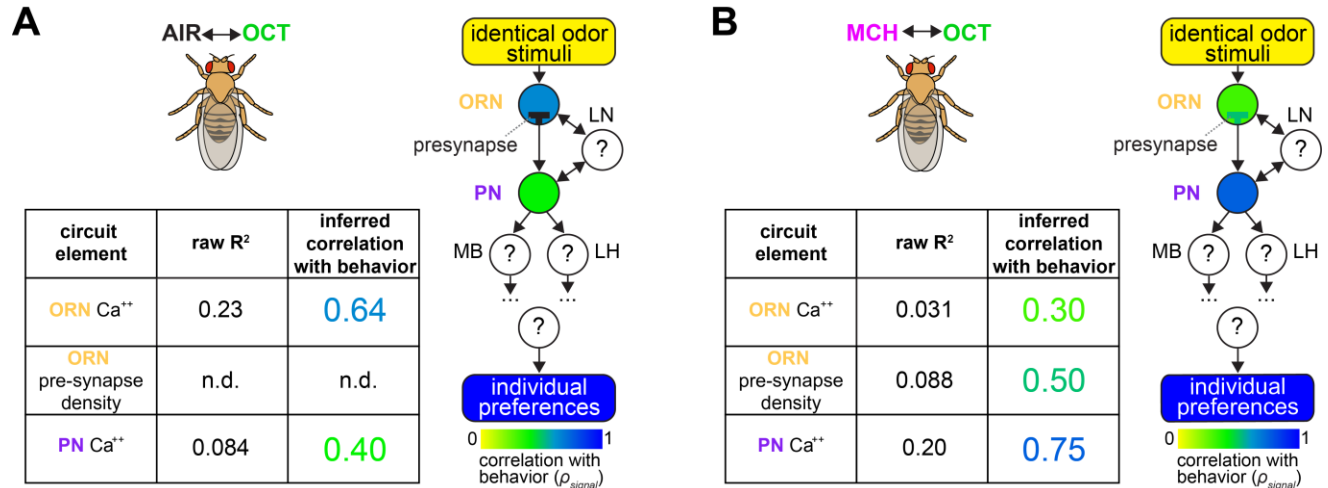
1341

1342

1343

**Figure 3 – figure supplement 2. Calcium and Brp-Short predictor variation.**

(A) Histogram of average PN  $\Delta f/f$  across all coding dimensions in flies in which OCT-AIR preference was measured (top) and OCT-AIR preference versus average PN  $\Delta f/f$  (n=53 flies) (bottom). (B) Similar to (A) for ORN  $\Delta f/f$  and OCT-AIR preference (n=30 flies). (C) Similar to (A) for  $\Delta f/f$  difference between DM2 and DC2 PN responses and OCT-MCH preference (n=69 flies). (D) Similar to (A) for % Brp-Short density difference between DM2 and DC2 ORNs and OCT-MCH (n=53 flies).

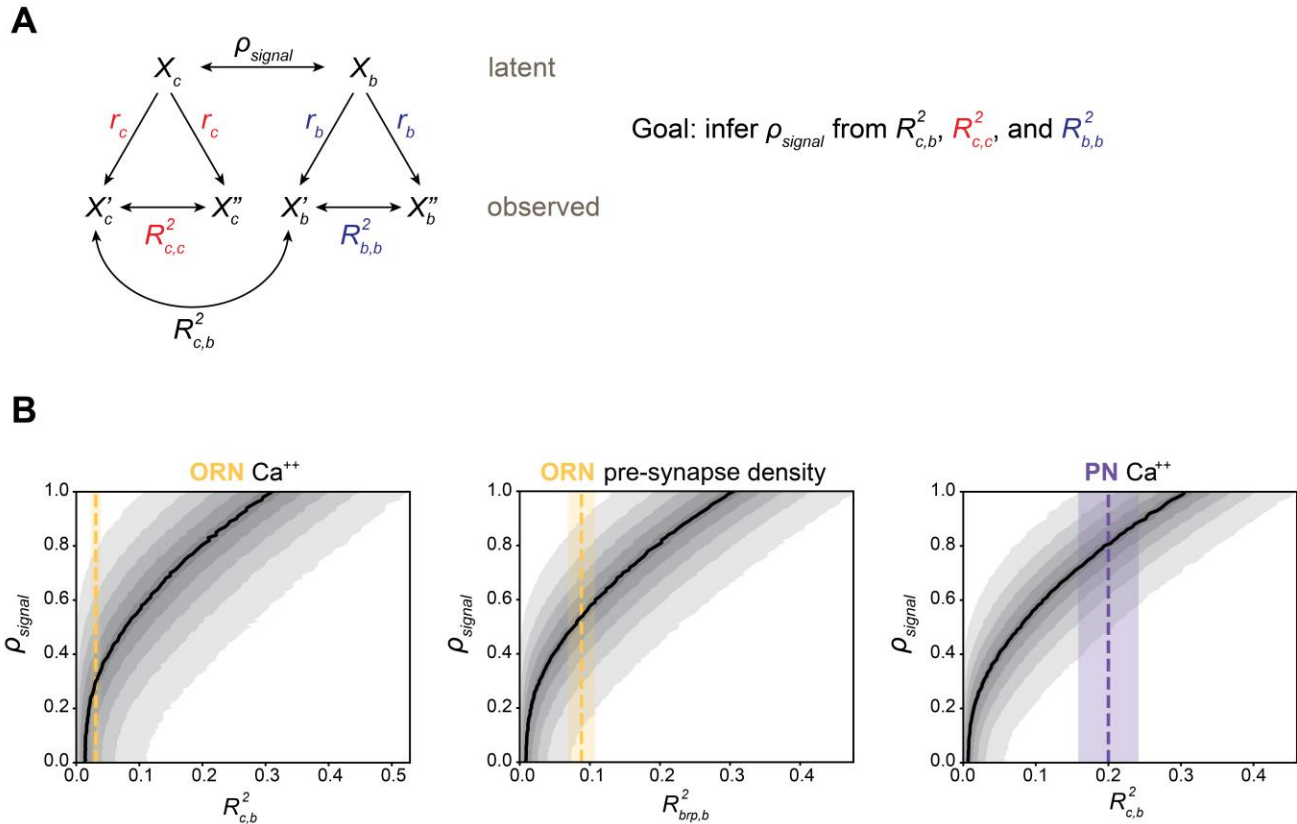


1344  
1345  
1346  
1347  
1348  
1349  
1350  
1351  
1352  
1353  
1354

**Figure 4. Loci of individuality across the olfactory periphery.**

(A) Table summarizing circuit element predictors, the strength of their nominal correlation with odor-vs-air behavior scores, and the inferred correlation between latent calcium / latent behavior. See analysis in Figure 4 – figure supplement 1. Schematic at right places these values in the context of the olfactory circuit. ORN Ca<sup>++</sup> corresponds to PC 1 of ORN calcium (Figure 1L), PN Ca<sup>++</sup> corresponds to PC1 of PN calcium (Figure 1M; trained model applied to train+test data). (B) As in (A) but for odor-vs-odor experiments. ORN Ca<sup>++</sup> corresponds to PC 1 of ORN calcium (Figure 1O), ORN pre-synapse density corresponds to PC2 of Brp-Short relative fluorescence (Figure 3F; trained model applied to train+test data), PN Ca<sup>++</sup> corresponds to PC 2 of PN calcium (Figure 1P; trained model applied to train+test data).

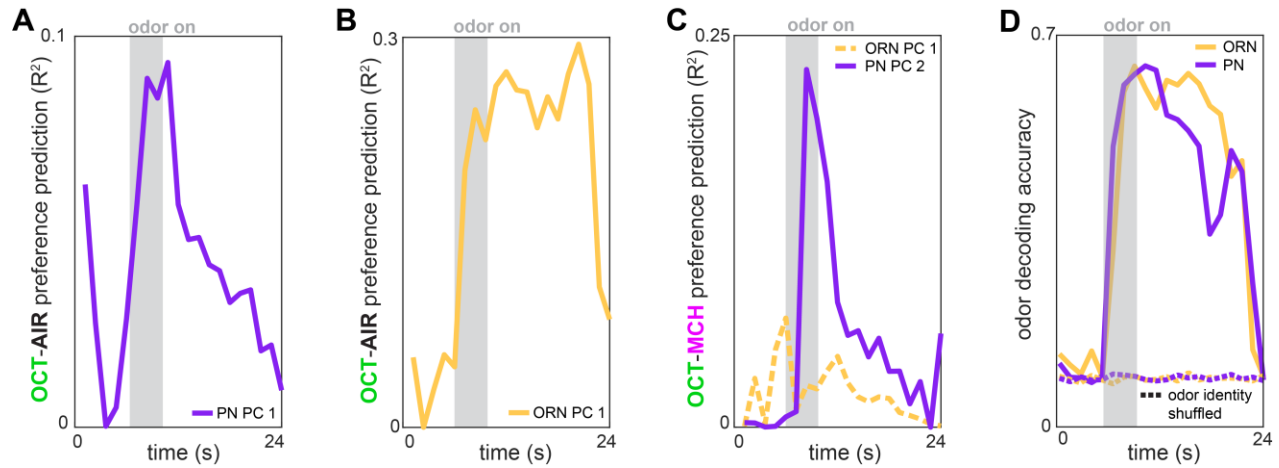




1355  
1356  
1357  
1358  
1359  
1360  
1361  
1362  
1363  
1364  
1365  
1366  
1367  
1368  
1369  
1370

**Figure 4 – figure supplement 1. Estimating latent calcium - behavior correlations.**

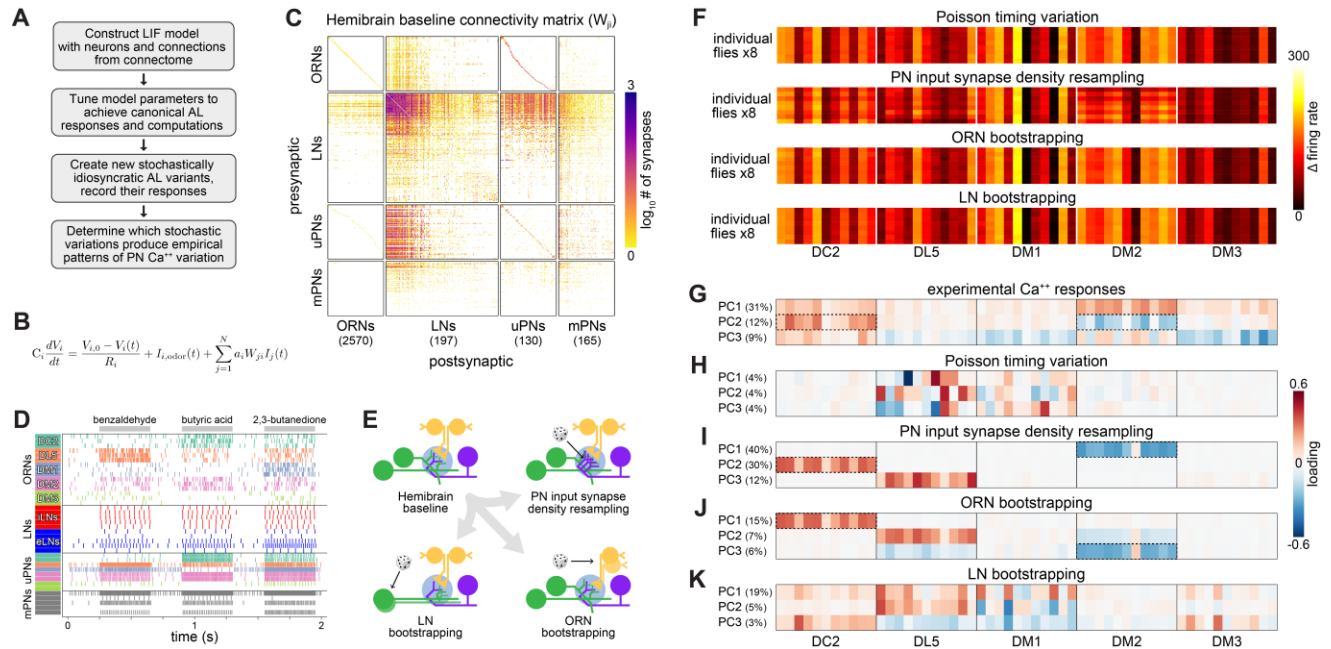
(A) Schematic of inference approach to estimate the correlation between latent calcium (c) and behavioral (b) states ( $\rho_{signal}$ ). This method can be applied identically to infer  $\rho_{signal}$  between Brp measurements and behavior. (B) Demonstration of  $\rho_{signal}$  inference for OCT vs MCH models presented in Figure 4: ORN calcium PC 1 (left,  $N=30$ ,  $R^2=0.25$  indicated in dashed line), ORN Brp-Short PC 2 from trained model applied to train+test data (middle,  $N=53$ ,  $R^2=0.088$  indicated in dashed line), PN calcium PC 2 from trained model applied to train+test data (right,  $N=69$ ,  $R^2=0.20$ ). Black line indicates median  $R_{c,b}^2$  ( $R_{brp,b}^2$  for Brp-Short model) among the 10,000 simulations for each  $\rho_{signal}$ , shaded areas (from lightest to darkest to lightest) indicate 5-15th, 15-25th, ..., 85-95th percentile  $R_{c,b}^2$  ( $R_{brp,b}^2$ ). The marginal distribution for  $\rho_{signal}$  was estimated as the distribution of simulations for each  $\rho_{signal}$  for which the simulated  $R_{c,b}^2$  ( $R_{brp,b}^2$ ) had a value +/- 20% of the linear models'  $R^2$  (dashed lines). For the examples depicted here, the median  $\rho_{signal}$  for ORN calcium PC1 was 0.30 (90% CI as estimated by the 5th-95th percentiles of the marginal distribution: 0.02-0.74), for ORN Brp-Short PC 2: 0.50 (0.11-0.85), for PN PC 2: 0.75 (0.44-0.96).



1371  
1372  
1373  
1374  
1375  
1376  
1377  
1378  
1379

**Figure 4 – figure supplement 2. Time-dependent preference- and odor-decoding.**

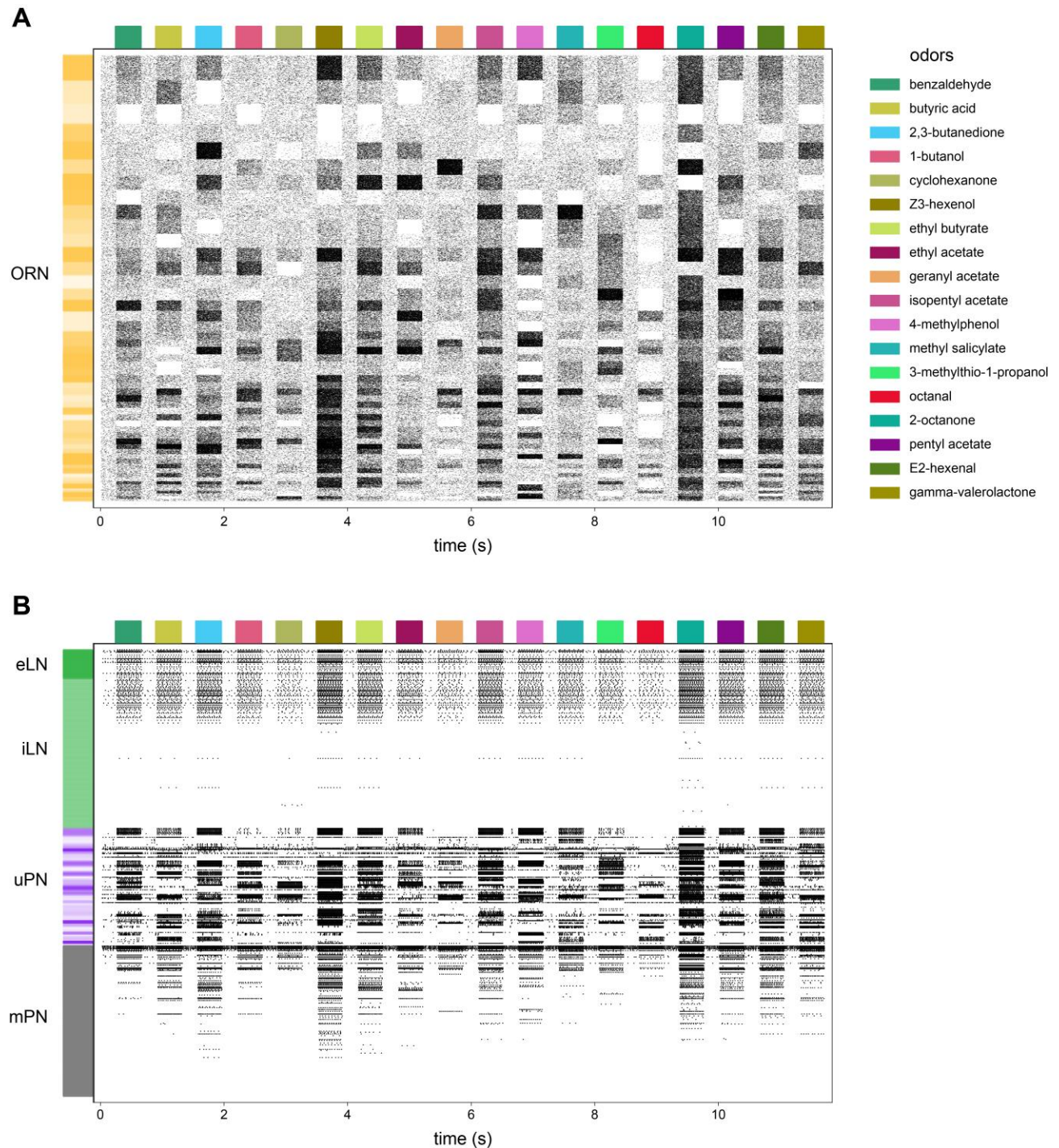
(A) R<sup>2</sup> of odor-vs-air preference predicted by PC 1 of PN activity as a function of time across trials (n=53 flies). (B) R<sup>2</sup> of odor-vs-air preference predicted by PC 1 of ORN activity as a function of time across trials (n=30 flies). (C) R<sup>2</sup> of odor-vs-odor preference predicted by PC 2 of PN activity (solid plum, n=69 flies) or PC 1 of ORN activity (dashed peach, n=35 flies) as a function of time across trials. (D) Logistic regression classifier accuracy of decoding odor identity from 5 glomerular responses as a function of time. Dashed curves indicate performance on shuffled data.



1380  
 1381  
 1382  
 1383  
 1384  
 1385  
 1386  
 1387  
 1388  
 1389  
 1390  
 1391  
 1392  
 1393  
 1394  
 1395  
 1396  
 1397  
 1398  
 1399  
 1400

### Figure 5. Simulation of developmentally stochastic olfactory circuits

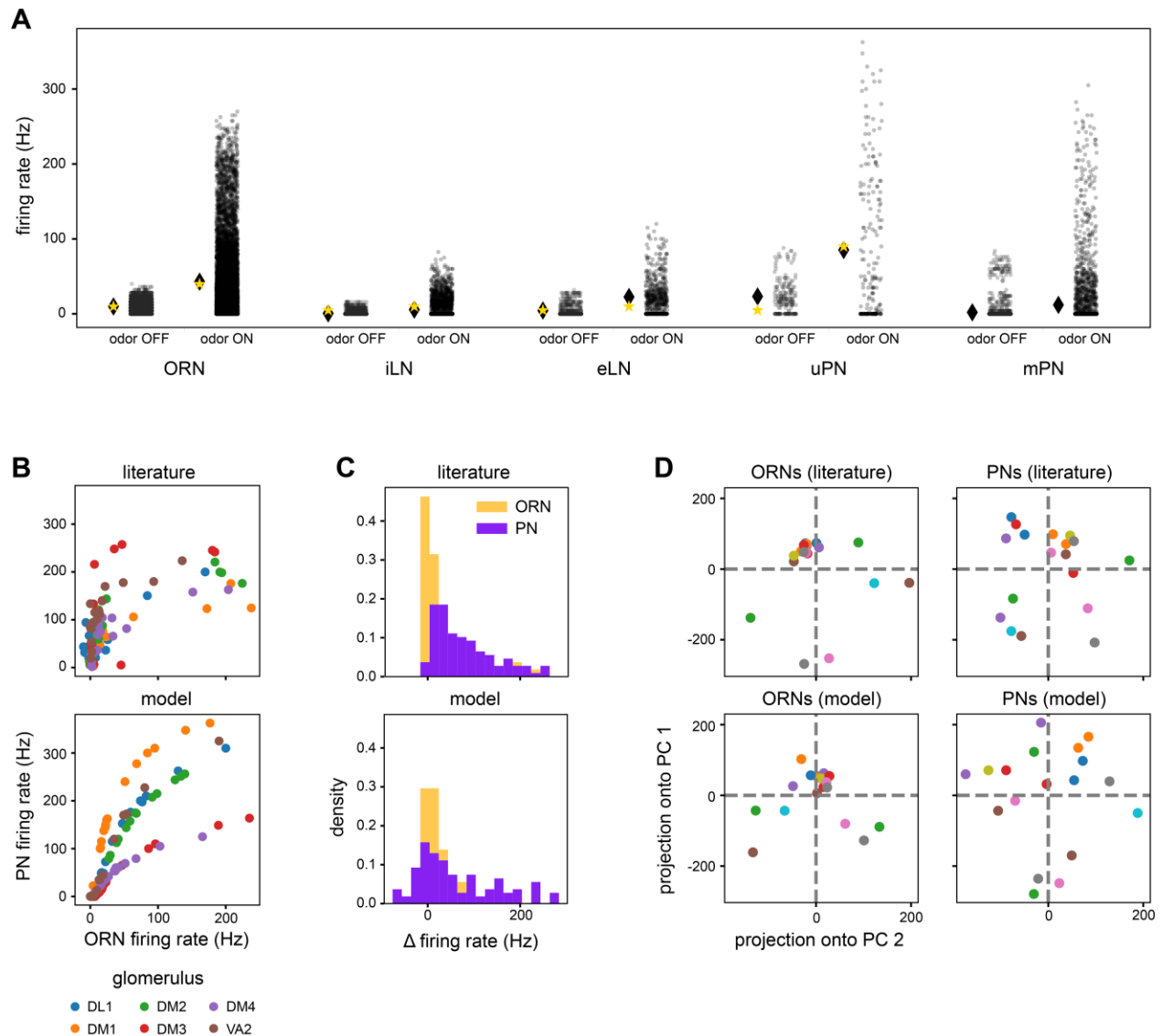
**(A)** AL modeling analysis outline. **(B)** Leaky-integrator dynamics of each simulated neuron. When a neuron's voltage reaches its firing threshold, a templated action potential is inserted, and downstream neurons receive a postsynaptic current. See *Antennal Lobe modeling* in Materials and Methods. **(C)** Synaptic weight connectivity matrix, derived from the hemibrain connectome (Scheffer et al., 2020). **(D)** Spike raster for randomly selected example neurons from each AL cell type. Colors indicate ORN/PN glomerular identity and LN polarity (i=inhibitory, e=excitatory). **(E)** Schematic illustrating sources of developmental stochasticity as implemented in the simulated AL framework. See Supplementary Video 4 for the effects of these resampling methods on the synaptic weight connectivity matrix. **(F)** PN glomerulus-odor response vectors for 8 idiosyncratic ALs subject to Input spike Poisson timing variation, PN input synapse density resampling, and ORN and LN population bootstrapping. **(G)** Loadings of the principal components of PN glomerulus-odor responses as observed across experimental flies (top). Dotted outlines highlight loadings selective for the DC2 and DM2 glomerular responses, which underlie predictions of individual behavioral preference. **(H-K)** As in (G) for simulated PN glomerulus-odor responses subject to Input spike Poisson timing variation, PN input synapse density resampling, and ORN and LN population bootstrapping. See Figure 5 – figure supplement 5 for additional combinations of idiosyncrasy methods. In (F-K) the sequence of odors within each glomerular block is: OCT, 1-hexanol, ethyl-lactate, 2-heptanone, 1-pentanol, ethanol, geranyl acetate, hexyl acetate, MCH, pentyl acetate and butanol.



1401  
1402 **Figure 5 – figure supplement 1. AL model raster plot.**

1403 (A) Action potential raster plot of ORNs in the baseline simulated AL. Rows are individual  
1404 ORNs, black ticks indicate action potentials. Random shades of orange at left indicate blocks of  
1405 ORN rows projecting to the same glomerulus. (B) The remaining neurons in the model. Shades  
1406 of green indicate excitatory vs inhibitory LNs and shades of purple indicate PNs with dendrites  
1407 in the same glomeruli.





1408

1409

1410 **Figure 5 – figure supplement 2. AL model baseline outputs compared to experimental data.**

1411 (A) Distributions of model neuron firing rates by cell type across odors (transparent black points

1412 are individual neuron-odor combinations). Black lozenge symbols indicate the mean firing rate

1413 of the points to the right. Yellow stars indicate the comparable experimental values reported in

1414 (Chou et al., 2010; de Bruyne et al., 2001; Nagel et al., 2015; Wilson, 2004). (B) Scatter plots of

1415 average PN firing rate vs ORN firing rate during odor stimuli in the model vs experimental

1416 values (Bhandawat et al., 2007). Points are odors, colors are glomeruli. (C) Histograms of ON

1417 odor minus OFF odor glomerulus-average PN and ORN firing rates in the model vs experimental

1418 values (Bhandawat et al., 2007), showing flatter distributions in PNs. (D) Odor representations in

1419 the first 2 PCs of glomerulus-average ORN responses and PN responses in the model and

1420 experimental results (Bhandawat et al., 2007). Points are odors. Pairwise distances between PN

1421 representations are more uniform than in ORNs in both the model and experimental data. Panels

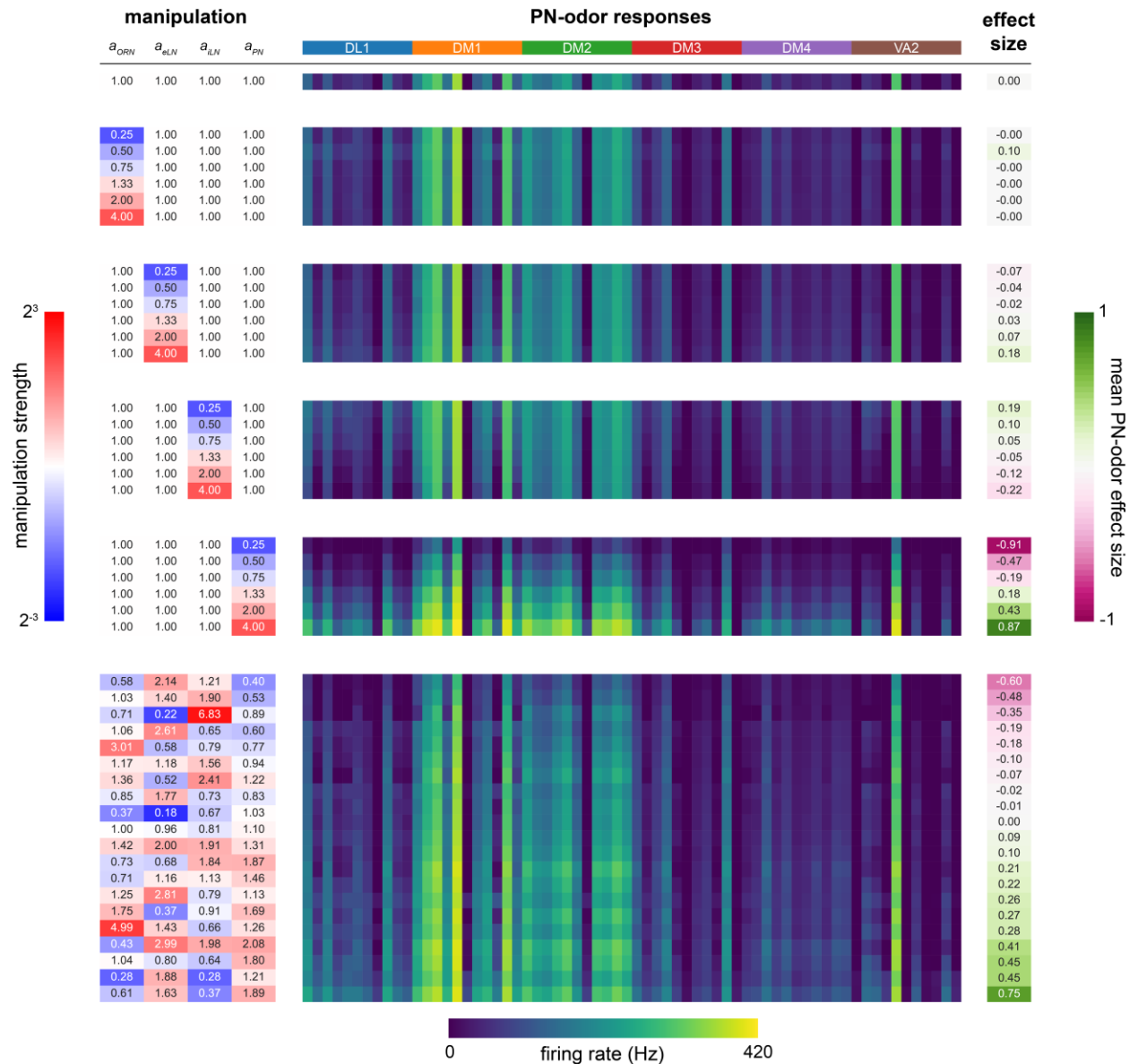
1422 (B)-(D) use glomerulus-average PN and ORN firing rates from six of the seven glomeruli in

1423 Bhandawat et al., 2007, as VM2 is significantly truncated in the hemibrain (Scheffer et al.,

1424 2020). Literature features in panels (B)-(D) were extracted from Bhandawat et al., 2007 using

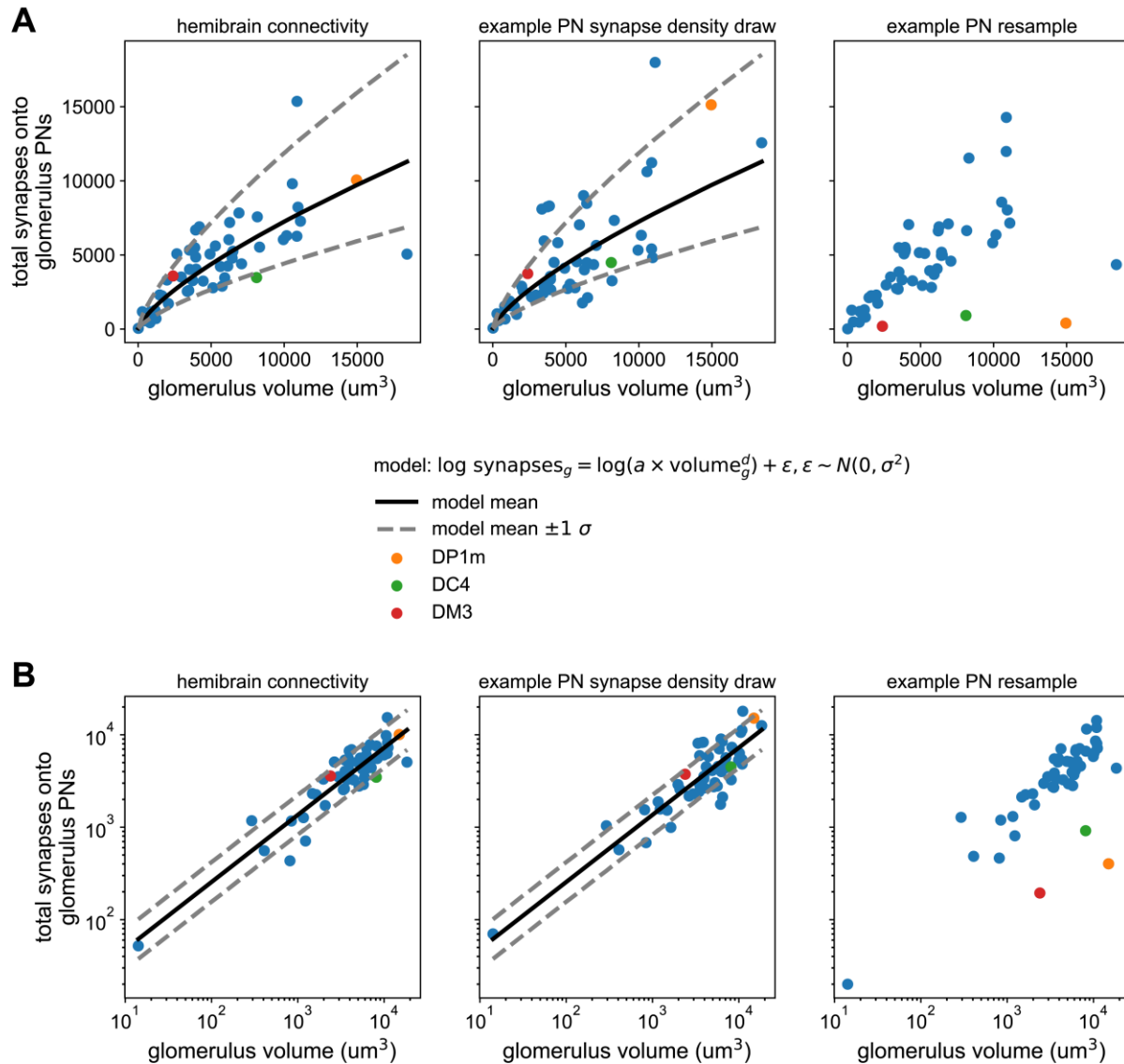
WebPlotDigitizer (Rohatgi, 2021).





1425 **Figure 5 – figure supplement 3. Sensitivity analysis of  $a_{ORN}$ ,  $a_{eLN}$ ,  $a_{iLN}$ ,  $a_{PN}$  parameters.**  
 1426 (Left, blue to red colormap): magnitude of parameter manipulation. (Center, dark blue to yellow  
 1427 colormap): mean glomerular firing rate (Hz) responses of PNs (DL1, DM1, DM2, DM3, DM4,  
 1428 VA2) to 11 odors (order within each glomerulus (colored bands at top): 3-octanol, 1-hexanol,  
 1429 ethyl lactate, 2-heptanone, 1-pentanol, ethanol, geranyl acetate, hexyl acetate, 4-  
 1430 methylcyclohexanol, pentyl acetate, 1-butanol, 3-octanol). (Right, pink to green colormap):  
 1431 manipulation effect size on mean PN-odor responses (Cohen's  $d$ ). (Top): baseline parameter set.  
 1432 (Middle): single-parameter manipulations from 1/4x to 4x. (Bottom): multiple-parameter  
 1433 manipulations. For further detail see *AL model tuning* in Materials and Methods. No  
 1434 manipulations yielded effect sizes larger than 0.9;  $a_{PN}$  is the most sensitive parameter.  
 1435

1436



1437

1438

1439

**Figure 5 – figure supplement 4. Synapse counts vs glomerular volume in the hemibrain and AL model.**

1440 (A) Left) Scatter plot of total PN input synapses within a glomerulus vs that glomerulus' volume

1441 from the hemibrain data set. Solid line represents the maximum likelihood-fit mean synapse

1442 count vs glomerular volume, and dashed lines the fit  $\pm 1$  standard deviation. Middle) As (left)

1443 but for a single sample from the parameterized distribution of PN input synapses vs glomerular

1444 volume. Right) As in previous for a single bootstrap resample of PNs. Color-highlighted

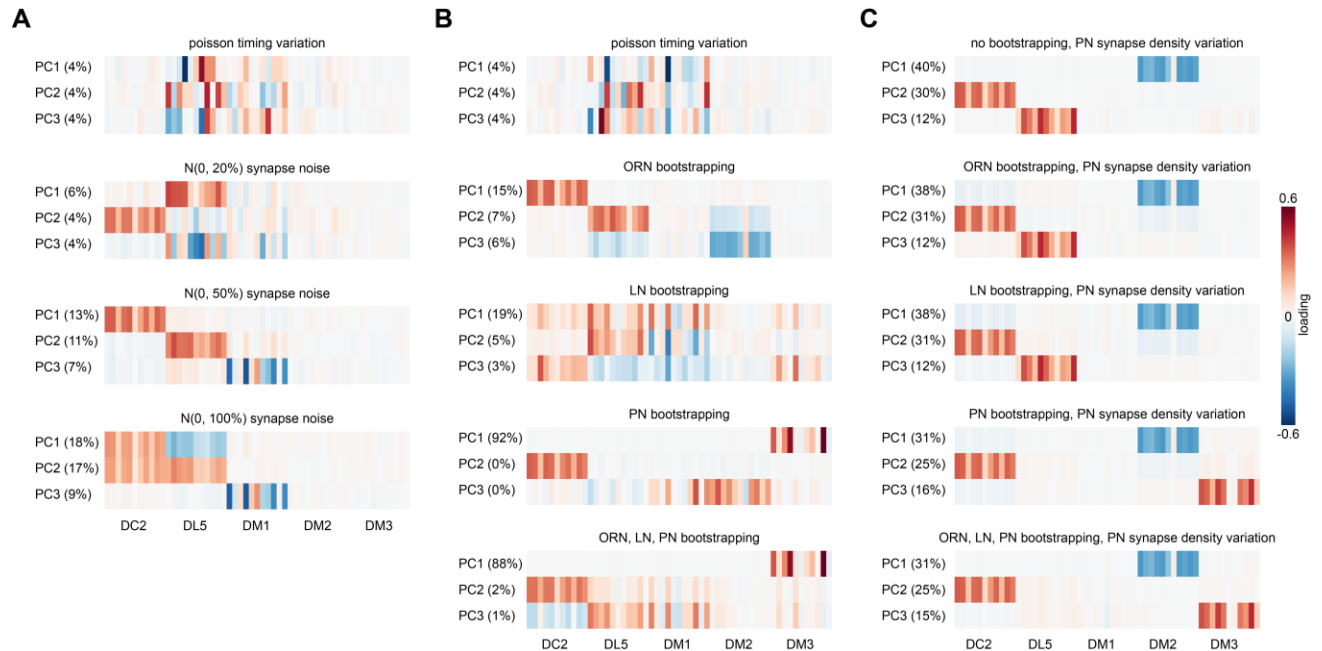
1445 glomeruli illustrate that when PNs within a glomerulus have highly asymmetrical synapse

1446 counts, bootstrapping them alone can result in apparent synapse densities that lie outside the

1447 empirical distribution (left). (B) As in (A) but on log-log axes, showing the linear relationship

1448 between synapse density and glomerular volume after this transformation, and bootstrapped

1449 densities falling outside this distribution at right.



1450

1451

1452

**Figure 5 – figure supplement 5. PN response PCA loadings under various sources of circuit idiosyncrasy.**

1453

1454

1455

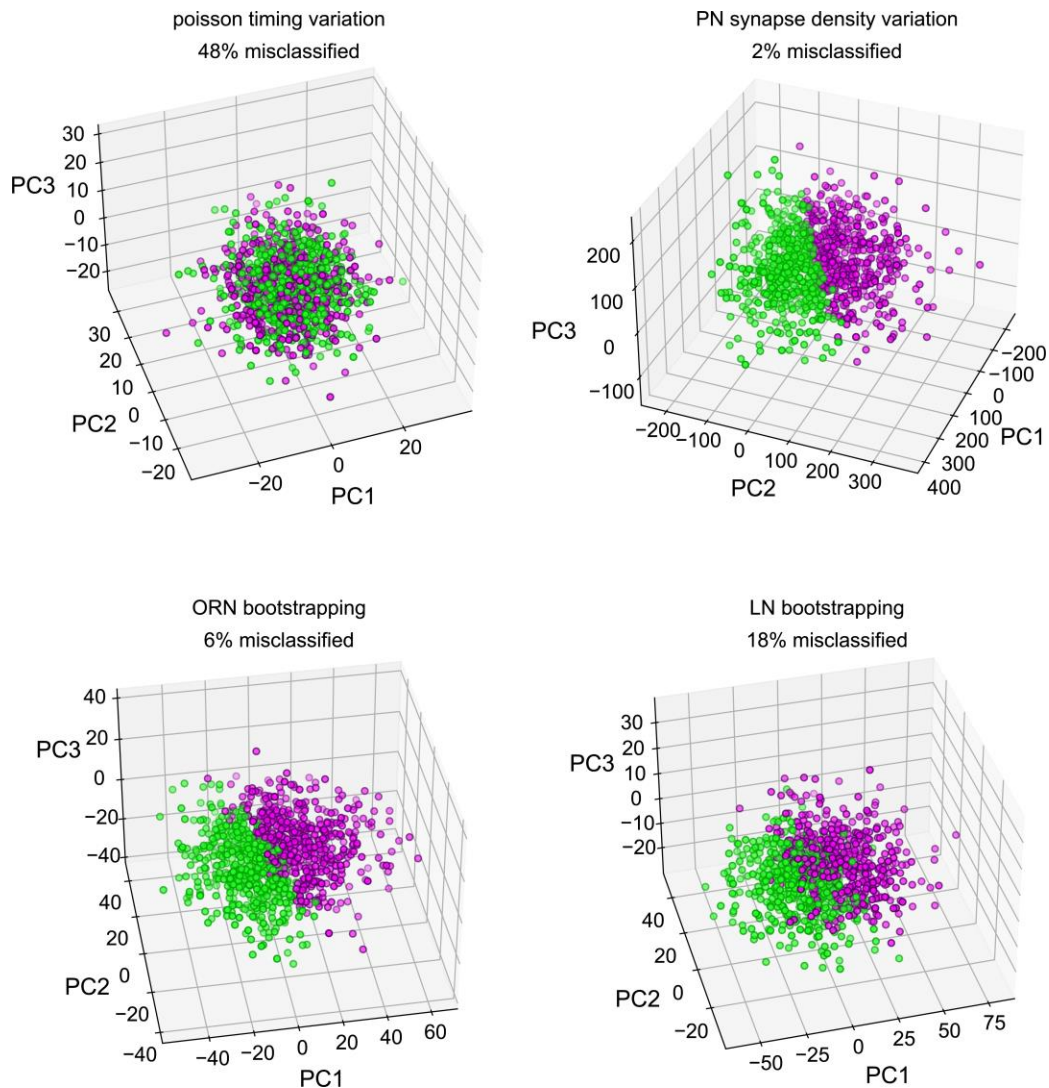
1456

1457

1458

(A) Loadings of the principal components of PN glomerulus-odor responses as simulated across AL models where Gaussian noise with a standard deviation equal to 0, 20, 50, and 100% of each synapse weight was added to each synaptic weight in the hemibrain data set. (B) circuit variation coming from bootstrapping of each major AL cell type or all three simultaneously. (C) circuit variation coming from bootstrap resampling of different cell-type combinations in addition to PN input synapse density resampling as illustrated in Figure 5 – figure supplement 4.

1459



1460

1461 **Figure 5 – figure supplement 6. Classifiability of simulated idiosyncratic behavior under**  
1462 **different sources of circuit idiosyncrasy.**

1463 Simulated PN odor-glomerulus firing rates projected into their first three principal components.

1464 Individual points represent single runs of resampled AL models, under four different sources of  
1465 idiosyncratic variation. PN responses in all odor-glomerulus dimensions were used to calculate  
1466 simulated behavior scores for each resampled AL, by applying the PN calcium-odor-vs-odor  
1467 linear model (Figure 2G). Magenta points represent flies with simulated preference for MCH in  
1468 the top 50%, and green OCT preference. % Misclassification refers to 100% – the accuracy of a  
1469 linear classifier trained on MCH-vs-OCT preference in the space of the first three PCs. This  
1470 measures how much of the variance along the PN calcium-odor-vs-odor linear model lies outside  
1471 the first three PCs of simulated PN variation.

1472 **Tables**

1473

1474 **Table 1: Calcium & Brp-Short – behavior model statistics**

Behavior Measured	Neural Predictor	Figure Panel	n	$\beta_0$	$\beta_1$	R <sup>2</sup>	p-value
OCT vs. AIR	PN Calcium PC 1 (Figure 2A)	Figure 2 – figure supplement 1A	18	-0.26	-0.079	0.16	0.099
OCT vs. AIR	PN Calcium Average all dimensions	2C	53	-0.051	-0.38	0.098	0.022
OCT vs. AIR	ORN Calcium PC 1 (Figure 2D)	1L	30	-0.29	-0.053	0.23	0.007
OCT vs. AIR	ORN Calcium Average all dimensions	2F	30	-0.032	-0.71	0.25	0.005
OCT vs. MCH	PN Calcium PC 2 (Figure 2G)	Figure 2 – figure supplement 1C	47	-0.058	-0.081	0.15	0.006
OCT vs. MCH	PN Calcium DM2 - DC2 (% difference)	2I	69	-0.032	-0.0018	0.12	0.004
OCT vs. MCH	ORN Calcium PC 1	1O	35	-0.14	-0.027	0.031	0.32
OCT vs. MCH	ORN Brp-Short PC 2 (train data only) (Figure 3E)	Figure 3 – figure supplement 1I	22	-0.087	0.017	0.22	0.028
OCT vs. MCH	ORN Brp-Short PC 2 (all data)	3F	53	-0.019	0.012	0.088	0.031
OCT vs. MCH	ORN Brp-Short DM2 - DC2	3G	53	-0.051	-0.007	0.053	0.096

1475

1476

**Table 2: Typical electrophysiology features of AL cell types, used as model parameters**

Parameter	ORNs	LN <sub>s</sub>	PN <sub>s</sub>
Membrane resting potential	-70 mV (Dubin and Harris, 1997)	-50 mV (Seki et al., 2010)	-55 mV (Jeanne and Wilson, 2015)
Action potential threshold	-50 mV (Dubin and Harris, 1997)	-40 mV (Seki et al., 2010)	-40 mV (Jeanne and Wilson, 2015)
Action potential minimum	-70 mV (Cao et al., 2016)	-60 mV (Seki et al., 2010)	-55 mV (Jeanne and Wilson, 2015)
Action potential maximum	0 mV (Dubin and Harris, 1997)	0 mV (Seki et al., 2010)	-30 mV (Wilson and Laurent, 2005)
Action potential duration	2 ms (Jeanne and Wilson, 2015)	4 ms (Seki et al., 2010)	2 ms (Jeanne and Wilson, 2015)
Membrane capacitance	73 pF (assumed = PN <sub>s</sub> )	64 pF (Huang et al., 2018)	73 pF (Huang et al., 2018)
Membrane resistance	1.8 GOhm (Dubin and Harris, 1997)	1 GOhm (Seki et al., 2010)	0.3 GOhm (Jeanne and Wilson, 2015)

1477



1478 **Supplementary Videos**

1479

1480 **Supplementary Video 1. Example recording with automated tracking of an odor-vs-air**  
1481 **behavioral assay.**

1482 The recent positions of each fly (green line) are shown in different colors. Red bar indicates  
1483 when the odor stream is turned on.

1484

1485 **Supplementary Video 2. Example recording with automated tracking of an odor-vs-odor**  
1486 **behavioral assay.**

1487 The recent positions of each fly (green line) are shown in different colors. Magenta and green  
1488 bars at right indicate when MCH and OCT are respectively flowing into the top and bottom  
1489 halves of each arena.

1490

1491 **Supplementary Video 3. Confocal image stack of expanded DC2>Brp-Short.**

1492 Magenta is nc82 stain, Green is Or13a>Brp-Short. Frames are z-slices spaced at 0.54  $\mu\text{m}$ . Image  
1493 height corresponds to a post-expansion field of view of 107 x 90  $\mu\text{m}$  (a  $\sim 2.5$  x linear expansion  
1494 factor).

1495

1496 **Supplementary Video 4. Simulated AL connectivity matrices.**

1497 Left: Glomerular density resampling. Each frame corresponds to the hemibrain connectome  
1498 synaptic weights, rescaled according to a sample from the relationship between synapse count  
1499 and volume parameterized in Figure 5 – figure supplement 4. Middle: ORN bootstrapping. Each  
1500 frame corresponds to the hemibrain connectome synaptic weights, but with the population of  
1501 ORNs projecting to each glomerulus resampled with replacement. Right: LN bootstrapping.  
1502 Each frame corresponds to the hemibrain connectome synaptic weights, but with the population  
1503 of LNs resampled with replacement.